International Journal of Heat and Mass Transfer 200 (2023) 123537

Contents lists available at ScienceDirect

International Journal of Heat and Mass Transfer

journal homepage: www.elsevier.com/locate/hmt

A modified Euler-Lagrange-Euler approach for modelling homogeneous and heterogeneous condensing droplets and films in supersonic flows

Hongbing Ding[a], Yu Zhang[a], Yan Yang[b], Chuang Wen[c,*]

[a] Tianjin Key Laboratory of Process Measurement and Control, School of Electrical and Information Engineering, Tianjin University, Tianjin 300072, China
[b] Faculty of Engineering, University of Nottingham, Nottingham NG7 2RD, United Kingdom
[c] Faculty of Environment, Science and Economy, University of Exeter, Exeter EX4 4QF, United Kingdom

ARTICLE INFO

Article history:
Received 1 July 2022
Revised 31 August 2022
Accepted 11 October 2022

Keywords:
Nucleation
Condensation
Liquid film
Droplet
Heat and mass transfer
Euler-Lagrange approach
Euler film model

ABSTRACT

The phase change in supersonic flows is of great interest in many industrial applications including steam turbines, nozzles, ejectors and aircraft. However, the phase change phenomenon is still not fully understood due to the completed flow behavior including nucleation, condensation, film generation and shock waves in supersonic flows. In the present study, we proposed a modified Euler-Lagrange-Euler model to explore the internal flow mechanism within supersonic separators. The mutual heat and mass transfer of the gaseous phase, droplets, and liquid film were simulated in supersonic flows. The homogeneous nucleation and growth model was innovatively added to ensure the model's comprehensiveness. The feasibility of the proposed model was validated by experiments. Then, the interaction of heterogeneous and homogeneous condensation in supersonic condensation flow was excavated for the first time. The results show the heterogeneous droplet diameter's decrease or concentration's increase had a significant inhibitory effect on homogeneous condensation. Subsequently, the supersonic swirl field's generation, the dynamic evolution of the homogeneous/heterogeneous droplet condensation and deposition, the liquid film development, and the heat-mass transfer between them in the supersonic separator were analyzed using the proposed model. Furthermore, the separation capacity of the supersonic separator was evaluated considering the co-action of homogeneous and heterogeneous condensation. Results show that increasing inlet droplet concentration from 0.0001 kg/s to 0.0025 kg/s can increase vapor separation efficiency and dew point depression from 61.39 % to 84.74 % and 19.03 K to 28.28 K, respectively.

1. Introduction

The deterioration of environmental problems and the complexity of the energy structure on a global scale have attracted gradual attention [1]. As an alternative energy source for oil and coal, the clean utilization of natural gas with low carbon dioxide emissions offers an opportunity to improve environmental quality [2,3]. The world's demand for natural gas has accelerated the development of natural gas processes [4]. However, the efficient separation and extraction of condensable gases and impurities in natural gas is still an urgent problem in the natural gas process [5]. The long-term presence of these impurity gases will cause blockages in natural gas transportation pipelines and even major safety accidents [6]. Supersonic separation is an emerging technology for natural gas purification [7]. Widespread attention has been quickly gained because of its advantages of strong separation ability [8], non-chemical properties [1], simple structure [9], and low cost [10]. Correspondingly, numerical studies on the flow properties of supersonic separators are also emerging to obtain higher purity natural gas [11–13].

The two key technologies for supersonic separation are cryogenic condensation and swirl separation [14]. As shown in Fig. 1, the wet gas is converted into swirling gas by the swirl generator [15]. Then the swirling gas passes through the supersonic nozzle to reach supersonic speed and generate a temperature drop. The water vapor begins to condense into droplets, and the droplets will hit the wall under the action of swirling flow to form a liquid film, the liquid film flows along the pipe wall and is eventually separated [16]. The gas phase flows axially in the pipe center in the form of continuous phase, part of the liquid phase flows axially along the pipe inner wall in the form of thin liquid film, and the other part of the liquid phase exists in the gas core in the form of entrainment droplet. This flow mode is called annular flow. However, the annular flow in supersonic separators is more complex for its supersonic, swirling, and condensing properties [17,18]. On

* Corresponding author.
E-mail address: c.wen@exeter.ac.uk (C. Wen).

https://doi.org/10.1016/j.ijheatmasstransfer.2022.123537

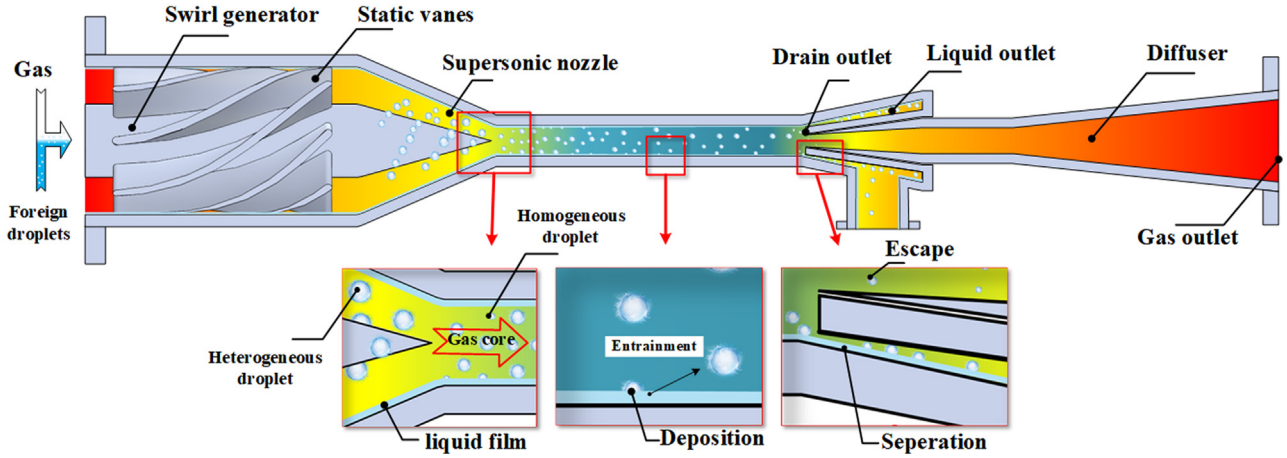

Fig. 1. Typical structure and physical process of a supersonic separator.

the one hand, both the homogeneous condensation inside the supersonic separator and the heterogeneous growth of the foreign droplet core will greatly change the annular flow field [19]; On the other hand, complex phenomena such as phase slip, deposition, entrainment, and swirl flow also bring many uncertainties to the development of the flow field [20]. Therefore, it is necessary to conduct a comprehensive mathematical model of this supersonic swirling annular flow with condensation to clarify the development mechanism.

Up to now, four feasible numerical methods have been demonstrated in the literature, namely, the Euler-Euler method, the Euler-Lagrange method, the Euler-Euler-Euler method, and the Euler-Lagrange-Euler method [18]. Both the gas phase and the droplets are treated as continuous phases by the Euler-Euler approach and solved using Euler's equations. Evaporation and condensation can be well calculated using the Euler-Euler model [21]. Dykas and Wróblewski [22] used the Euler-Euler method to simulate the homogeneous condensation flow in a low-pressure and high-pressure supersonic nozzle and studied the gas-liquid performance of the nozzle. On this basis, the drag model was revised, and the interphase slip was taken into account in the Euler-Euler model [23]. Liu et al. [24] established an Euler-Euler mathematical model for methane-steam condensation and studied the energy separation and condensation characteristics of wet natural gas. The results show that the interaction of the shock wave with the boundary layer reduces the liquefaction efficiency. Wen et al. [8,10] studied the flow field structure when homogeneous condensation and shock coexisted in supersonic flow and analyzed the effect of swirl intensity on the condensation process. Shooshtari and Shahsavand [25] established an Euler-Euler model considering homogeneous/heterogeneous condensation. The effect of heterogeneous salt particles on the condensation and separation of the supersonic separator was discovered. Taking interphase slip and droplet drag into account, the behavior of homogeneous/heterogeneous droplets in a supersonic separator was further complemented by Ding et al. [26]. The results show a moderate size of heterogeneous droplets can ensure optimal separation performance.

Unlike the Euler-Euler model, the Euler-Lagrange model employs a Lagrange approach to simulate the motion of droplets. Trajectories of individual droplets, as well as collisions between multiple droplets, can be easily traced [27]. Wen et al. [28] used the Euler-Lagrange model to numerically calculate the natural gas flow field and particle separation characteristics in a supersonic cyclone. The motion trajectories of particles with different particle sizes were predicted. Combined with the Euler-Lagrange model, Liu et al. [29] established a three-dimensional fluid numerical model of the supersonic separator. The effects of different structural parameters and operating conditions on the separation efficiency were investigated. Bai et al. [30] used the Euler-Lagrange method to simulate the particle-laden supersonic branching flow. the key features of the supersonic branching flow were revealed in the research. Yang and Wen [31] studied particle motion in strongly swirling supersonic flow. The results show that the gas flow is accelerated to supersonic speeds, creating low pressure and temperature conditions for gas removal. Wang et al. [32] employed the Euler-Lagrange model to predict the droplet trajectory and separation efficiency of the supersonic separator. The results show that with the increase of the droplet size, the separation efficiency gradually increases, and the particle size of 2–4 μm is more sensitive to the separation.

It can be seen that the Euler-Euler model and Euler-Lagrange methods are two widely used methods at present. However, although numerous studies have demonstrated the availability of the two models, the Euler-Euler model and Euler-Lagrange methods have the limitation that only the motion of the gas and droplets are calculated [16,18]. The formation and development of the liquid film on the wall are simplified or not considered, which means that the two models are actually inaccurate when simulating supersonic annular flow. To solve this problem, the exploration of coupling the two models with the liquid film model begins [33,34]. Li and Anglart [35] used the Euler-Euler model to simulate the gas core (gas, droplet) flow and used the Euler liquid film model to simulate the liquid film when studying the two-phase boiling flow. Simulation results show that dramatic temperature excursions can be well captured by the model. Chen et al. [36] proposed a combined Euler-Euler model and film model to simulate the paint deposition process when spraying a curved surface with a moving spray gun. Yue et al. [37] used a similar mathematical model to study the effect of liquid flow velocity on liquid film flow in Gas-Liquid Cylindrical Cyclone. The results show that the high liquid flow rate impairs the uniformity of the liquid film. Ding et al. [16] proposed a coupled model of the Euler-Euler model and the Euler liquid film model to simulate the swirl annular flow in a supersonic separator, taking into account the effects of homogeneous and heterogeneous condensation. The results show that with the increase of the inlet droplet concentration, the liquid film thickness, the interface wave frequency, and the interface wave velocity all increase. The Euler-Euler-Euler model has advantages in simulating supersonic condensation annular flow, and can comprehensively consider the changes of gas, droplet, and liquid film. However, there are problems in calculating discrete quantities such as single droplet trajectories, deposition of a single droplet, droplet

collision and coalescence, droplet and film breakup, etc., which are not conducive to further quantitative studies [37–39]. In contrast, the Euler-Lagrange-Euler method is based on the Euler-Lagrangian framework and is suitable for tracking local particles [40]. Yuan et al. [41] studied re-entrainment mechanisms of wall films. The gas core was solved by the Euler-Lagrange method, while the formation and stripping of the liquid film were studied using the Euler wall-film model. The average thickness and separation efficiency of the film decrease as the product of the viscosity and density of the continuous phase increases. Han et al. [20] established an Euler-Lagrange-Euler simulation model to study the gas-phase flow, droplet trajectories, and liquid film distributions of different separators in the PEMFC system. A separator structure more suitable for the PEMFC system was obtained. Deng et al. [18] successfully simulated the gas-liquid separation process in an axial flow cyclone using the Euler-Lagrangian method and the film model. The results indicated that the liquid film would cover the entire separation segment space over time.

As mentioned above, although the Euler-Euler, Euler-Lagrange, and Euler-Euler-Euler models have their advantages, the Euler-Lagrange-Euler model is the most suitable for simulating swirling annular flow. However, there has been no previous evidence for the Euler-Lagrange-Euler model to simulate the homogeneous condensation of droplets, and the Euler-Lagrange-Euler model has not been used in supersonic separators either. The performance of the model in high-speed condensation flow is unclear yet.

Therefore, to comprehensively study the properties of the gas, droplet, and liquid film in supersonic swirling condensation annular flow, as well as the heat-mass interaction between them, a modified Euler-Lagrange-Euler model was innovatively established. Not only was the Euler-Lagrange-Euler model introduced into the numerical study of supersonic separators, but the homogeneous condensation properties in the Euler-Lagrange-Euler model and its effect on flow were also calculated for the first time. The modeling ability of the established model was validated by experiments. The model was then used to study the condensation flow in a supersonic nozzle and the swirling condensation annular flow in a supersonic separator, respectively. The evolution and interaction of gas, droplets, and liquid film was discussed. Importantly, the interaction of homogeneous/heterogeneous condensation was explored. Finally, in the presence of homogeneous droplets, the improvement of the separation capacity by heterogeneous droplets in the supersonic separator was analyzed.

2. Modified Euler-Lagrange-Euler model

Swirling condensation annular flow in a supersonic separator was modeled using a coupled model of the Eulerian-Lagrangian method and the Eulerian liquid film model. The traditional Euler-Lagrange-Euler model cannot take homogeneous droplets into account, and also have shortcomings in considering complex mass and heat transfer characteristics. In this paper, the traditional Euler-Lagrange-Euler model has been modified to take homogeneous condensation into account in the mathematical model. This model also realizes a more accurate nucleation and growth model, which improves the deficiencies of the traditional Euler-Lagrange-Euler model in terms of mass and heat transfer. The modified Euler-Lagrange-Euler model mainly includes the control and tracking equations of gas, droplet, and liquid film, and the necessary coupling process between the three fields. As shown in Fig. 2, the model is based on the following assumptions:

(1) Ideal gas is used, and the condensable gas is water vapor;
(2) Homogeneous and heterogeneous condensation of droplets are considered;
(3) The droplets are considered spherical and can evaporate into water vapor;
(4) Collision, coalescence between droplets, and the breakup of droplets are considered;
(5) The droplet deposition, the film separation, and the film stripping are considered;
(6) The gas-film interaction is mainly evaporation and condensation.

2.1. Modeling the gas, droplets, and liquid film

Reynolds-averaged Navier-Stokes (RANS) equations and species transport equation are used to predict the gas phase, including continuity equations, momentum and energy equations. The governing equations of the gas phase are expressed in the form of Eqs. (1)–(4):

$$\frac{\partial \rho_g}{\partial t} + \nabla(\rho_g \vec{v}_g) = M_{\mathrm{pg}} + M_{\mathrm{fg}} \tag{1}$$

$$\frac{\partial}{\partial t}(\rho_g \vec{v}_g) + \nabla(\rho_g \vec{v}_g \vec{v}_g) = -\nabla p_g + \nabla \cdot \left[\mu_g\left(\nabla \vec{v}_g + \nabla \vec{v}_g^{T} - \frac{2}{3}\nabla \vec{v}_g Kr\right)\right] + \rho_g \vec{g} + U_{\mathrm{pg}} + M_{\mathrm{fg}} \vec{v}_{\mathrm{f}} \tag{2}$$

$$\frac{\partial(\rho_g E)}{\partial t} + \nabla \cdot [\vec{v}_g(\rho_g E + p_g)] = \nabla \cdot \left(-\lambda_{eff}\nabla T + \tau_{eff} \cdot \vec{v}_g\right) + Q_{\mathrm{pg}} + M_{\mathrm{fg}} h_v \tag{3}$$

$$\begin{cases} \frac{\partial}{\partial t}(\rho_g y_{\mathrm{i}}) + \nabla \cdot (\rho_g \vec{v}_g y_{\mathrm{i}}) = -\nabla \cdot \vec{J_{\mathrm{i}}} + S_{\mathrm{i}} \\ \vec{J_{\mathrm{i}}} = -\left(\rho_g D_{\mathrm{i,m}} + \frac{\mu_t}{Sc_t}\right)\nabla y_{\mathrm{i}} - D_{\mathrm{T,i}} \frac{\nabla T}{T} \end{cases} \tag{4}$$

where ρ, $\vec{v}$, p, T are the density, velocity, pressure and temperature, respectively. The subscripts g, p, f and i stand for gas, droplet, liquid film and species. ∇ is the surface gradient operator. μ_g is the dynamic viscosity. Kr is Kronecker delta number. E is the total enthalpy, and h_v represents the latent heat of the water vapor. λ_{eff} and τ_{eff} are the effective thermal conductivity and effective stress tensor, respectively. y_{i} is the mass fraction of each species, $\vec{J_{\mathrm{i}}}$represents mass diffusion. S_{i} is the mass source term of the species in gas phase. M_{pg} and M_{fg} represent mass transfer (kg m^{-3} s^{-1}) from droplets and liquid film to the gas phase, respectively. U_{pg} and Q_{pg} represent momentum and energy transfer from droplets to gas. $D_{\mathrm{i,m}}$ is the mass diffusion coefficient for species i in the mixture, $D_{\mathrm{T,i}}$ is the thermal diffusion coefficient. Sc_{t} is the turbulent Schmidt number (0.7), μ_{t} and D_{t} are the turbulent viscosity and turbulent diffusivity.

The droplet trajectory equation can be calculated by

$$m_{\mathrm{p}} \frac{d\vec{v}_{\mathrm{p}}}{dt} = m_{\mathrm{p}}(\vec{v}_{\mathrm{g}} - \vec{v}_{\mathrm{p}}) \frac{18\mu}{\rho_{\mathrm{p}} d_{\mathrm{p}}^2 C_{\mathrm{c}}} + m_{\mathrm{p}} \vec{g} \tag{5}$$

where m_{p}, d_{p} are the droplet mass and diameter. C_{c} is the Cunningham correction to Stokes' drag law [42], which is described as:

$$C_{\mathrm{c}} = 1 + \frac{2\lambda_{\mathrm{mg}}}{d_{\mathrm{p}}}\left(1.257 + 0.4e^{-\frac{1.1 d_{\mathrm{p}}}{2\lambda_{\mathrm{mg}}}}\right) \tag{6}$$

where λ_{mg} is the mean free path of a gas molecule. Collision and coalescence between homogeneous and heterogenous droplets may occur when droplet paths cross, and the effect of such behavior on droplet properties is measured by O 'Rourke algorithm [43], which assumes that two droplets can collide only if they move into the same cell. When two droplets reach collision conditions, their likely fate is to coalesce, bounce or break up. When the homogeneous droplets collide with the heterogeneous droplets,

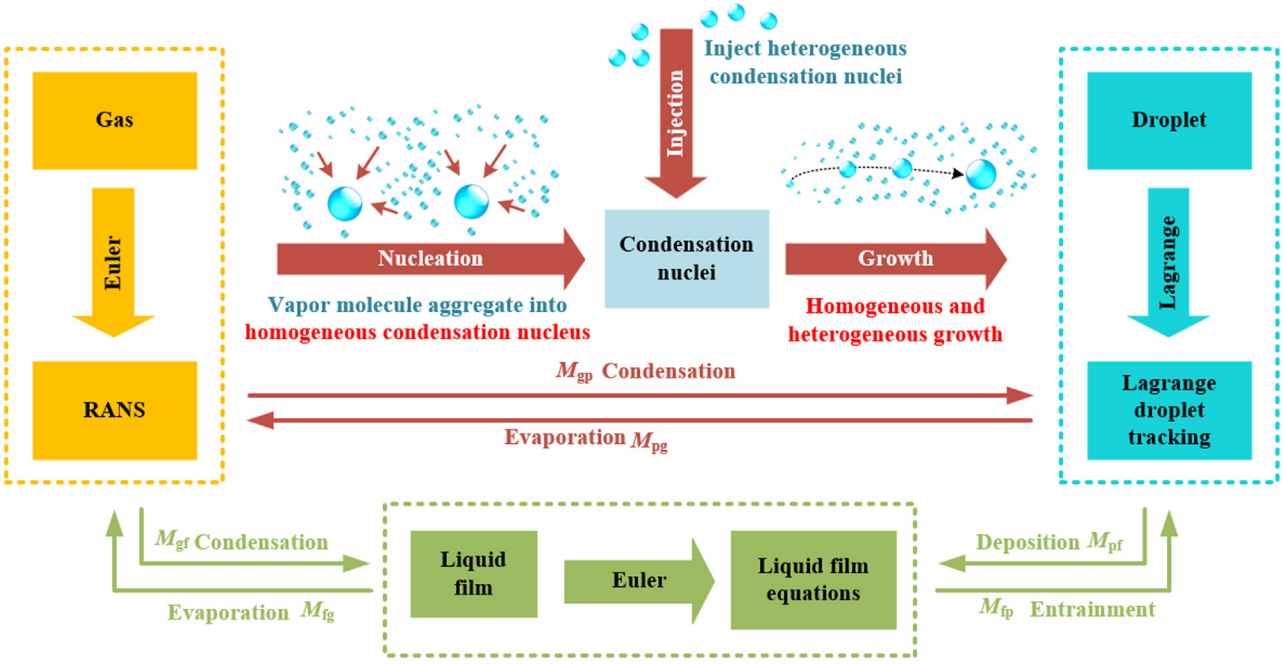

Fig. 2. Schematic diagram of the modified Euler-Lagrange-Euler model for modeling supersonic swirling condensation annular flow in the supersonic separator.

the huge particle size difference makes the homogeneous droplets very likely to be absorbed by the heterogeneous droplets, which depends on the final calculation result of the O'Rourke algorithm.

The Eulerian wall film model is used here to simulate the liquid film behavior. The governing equation for the liquid film is

$$\frac{\partial \rho_f \delta}{\partial t} + \nabla \cdot (\rho_f \delta \vec{v}_f) = \delta\left(M_{pf} + M_{gf}\right) \tag{7}$$

$$\frac{\partial \rho_f \delta \vec{v}_f}{\partial t} + \nabla \cdot (\rho_f \delta \vec{v}_f \vec{v}_f) = -\delta \cdot \nabla p_L + \delta \rho_f \vec{g}_\tau + \frac{3}{2}\tau_{f-g} - \frac{3\mu_f}{\delta}\vec{v}_f + \delta\left(M_{pf} + M_{gf}\right)\vec{v}_f \tag{8}$$

$$p_L = p_g \underbrace{-\rho\delta(\vec{n}\cdot\vec{g})}_{p_h} \underbrace{-\sigma\nabla\cdot(\nabla\delta)}_{p_\sigma} \tag{9}$$

$$\frac{\partial}{\partial t}(\rho_f \delta h_f) + \nabla \cdot (\rho_f \delta h_f \vec{v}_f) = \frac{\lambda_f}{\delta}(T_s + T_w - 2T_m) + \delta\left(M_{pf} + M_{gf}\right)h_v \tag{10}$$

where δ is the film thickness, M_{pf} and M_{gf} are the source terms from droplets and gas to liquid film [44]. $\vec{g}_\tau$ is the gravity component parallel to the film, $\tau_{f\text{-}g}$ is the viscous shear stress on gas-film interfaces, μ_f is the film dynamic viscosity. h_f is the film specific enthalpy, T_s, T_w, and T_m are the temperature of the film surface, wall, and film half-depth, respectively.

2.2. Modeling the droplet nucleation and growth

The mass and momentum transfers from the gas phase to the discrete droplet phase can be calculated by examining the change in mass and momentum of a droplet as it passes through each control volume [45]:

$$M_{gp} = \frac{\Delta m_p}{m_{p,0}}\frac{\dot{m}_{p,0}}{V_{cell}} \tag{11}$$

$$U_{gp} = \sum M_{gp}(\vec{v}_g - \vec{v}_p)\frac{18\mu}{\rho_p d_p^2 C_c} \tag{12}$$

where $m_{p,0}$ and $\dot{m}_{p,0}$are the initial mass (kg) and initial mass flow rate (kg s^{-1}) of droplets at the cell entry. V_{cell} is the cell volume. Δm_p represents the change in the droplet mass:

$$\Delta m_p = \begin{cases} m_{nucleation} + m_{growth}, & \text{for homogeneous droplet} \\ m_{growth}, & \text{for heterogeneous droplet} \end{cases} \tag{13}$$

where $m_{nucleation}$ is the droplet mass increase due to homogeneous nucleation, and m_{growth} is the droplet mass increase due to homogeneous or heterogeneous growth.

A single droplet nucleates and appears to produce a mass change of

$$m_{nucleation} = \frac{4}{3} I \rho_p \pi r_c^3 V_{cell} \Delta t \tag{14}$$

where Δt represents the time step, I is the nucleation rate (m^{-3} s^{-1}), and r_c is the critical nucleation radius of the droplet. The calculation equation for I and r_c are [16,46]

$$I = \frac{\upsilon_v n_v^2}{Ss}\sqrt{\frac{2\sigma}{\pi m_{molc}^5}}\exp\left(-\frac{16}{3}\frac{\pi \upsilon_v^2 \sigma^3}{(k_B T_v)^2 \ln(Ss)^2}\right) \tag{15}$$

$$r_c = \frac{2\sigma}{\rho_p R_v T_v \ln S_s} \tag{16}$$

where υ_v is the volume of a single liquid molecule, n_v is the molecular density of water vapor, and m_{molc} is the mass of the water molecule. k_B is the Boltzmann's constant (1.3807×10^{-23} J K^{-1}). R_v represents a specific gas constant of water vapor, T_v is water vapor temperature. S_s means supersaturation, equal to $p_v/p_{sat}(T_g)$, where p_{sat} is the water vapor saturation pressure at temperature T_g. σ is the liquid surface tension (N m^{-1}), which is calculated by [47]

$$\sigma = \left(85.27 + 75.612T_R - 256.889T_R^2 + 95.928T_R^3\right) \times 10^{-3} \tag{17}$$

where $T_R = T_g/T_c$ is the reduced temperature and T_c is the critical temperature (647.3 K).

The mass transfer of a single droplet due to homogeneous or heterogeneous droplet growth is

$$m_{growth} = \rho_p A_p \frac{dr}{dt}\Delta t \tag{18}$$

where A_p is the surface area of the droplet, r_p is the radius of the droplet, and the growth rate of both homogeneous and heterogeneous droplets is expressed as

$$\frac{dr_p}{dt} = \frac{\alpha}{\rho_p h_v}(T_r - T_v) \tag{19}$$

where T_r denotes the droplet surface temperature, α is the heat transfer coefficient. T_r and α are written as [48,49]

$$\alpha = \left(2 + 0.6\mathrm{Re}^{1/2}\right)\frac{\lambda_v}{2r_p}\frac{1}{1 + \frac{2\sqrt{8\pi}}{1.5\,\mathrm{Pr}} \times \frac{\Gamma_v}{1+\Gamma_v}Kn} \tag{20}$$

$$T_r = T_d - \frac{r_c}{r_p}(T_d - T_v) \tag{21}$$

where λ_v, Re, Pr, Kn, and Γ_v are the thermal conductivity of the vapor, Reynolds number, Prandtl number, Knudsen number, and specific heat ratio, respectively. T_d is the dew point temperature under local vapor pressure. During gas condensation, the temperature of the surrounding steam is always lower than the temperature of the droplet surface, which can be calculated using Eq. (21) for both homogeneous and heterogeneous droplets.

2.3. Modeling the droplet-film and gas-film mass-heat interactions

The calculation equation for M_{gf} in Eq. (7) is as follows [50]:

$$\delta M_{gf} = \frac{(\rho_m D_v/\delta)}{\rho_m D_v/\delta + C_{phase}} C_{phase}(y_v - y_{sat}) \tag{22}$$

$$C_{phase} = \begin{cases} C_{con}, & y_v > y_{sat} \\ C_{evap}\delta \cdot 10^4, & y_v < y_{sat} \end{cases} \tag{23}$$

where ρ_m is the density of the gas mixture, D_v ($m^2\ s^{-1}$) is the mass diffusivity of the water vapor, C_{phase} is the phase change constant, C_{con} and C_{evap} (kg $m^{-2}\ s^{-1}$) are condensation and evaporation constant. y_v represents the vapor mass fraction. The saturation vapor mass fraction y_{sat} is computed as:

$$y_{sat} = \frac{p_{sat}}{p_g}\frac{Mw_v}{Mw_m} \tag{24}$$

where Mw_i and Mw_m are the molecular weight of the species and the mixture. p_{sat} is only related to temperature, and is calculated as [51]:

$$\log_{10} p_{sat} = -2.1794 + 0.02953 \times T - 9.1837 \times 10^{-5} \times T^2 + 1.4454 \times 10^{-7} \times T^3 \tag{25}$$

The expression of M_{pf} in Eq. (7) is:

$$M_{pf} = M_{de} - M_{se} - M_{st} \tag{26}$$

M_{de} represents the mass exchange of droplet deposition. M_{se} is the mass source contributed by liquid film separation, which occurs near the separation port of the supersonic separator when the following two conditions are met:

$$\theta > \theta_c, We_f > We_c \tag{27}$$

where θ is the separation angle of the liquid outlet, We_f is the Weber number based on the film, and subscript c represents a critical value.

When the relative velocity between the gas core on the wall and the liquid film is high, Kelvin-Helmholtz waves form and grow on the film surface, eventually stripping droplets from the surface. This process is called film stripping, M_{st} are determined by the following equations [41]:

$$M_{st} = \frac{C \cdot 9 \cdot 3\sqrt{16} \cdot \pi\omega\rho_f}{V_{cell}}\left(\frac{\mu_f\sqrt{\sigma/\rho_f}}{\beta\rho_g\vec{v}_g^2}\right)^{2/3} \tag{28}$$

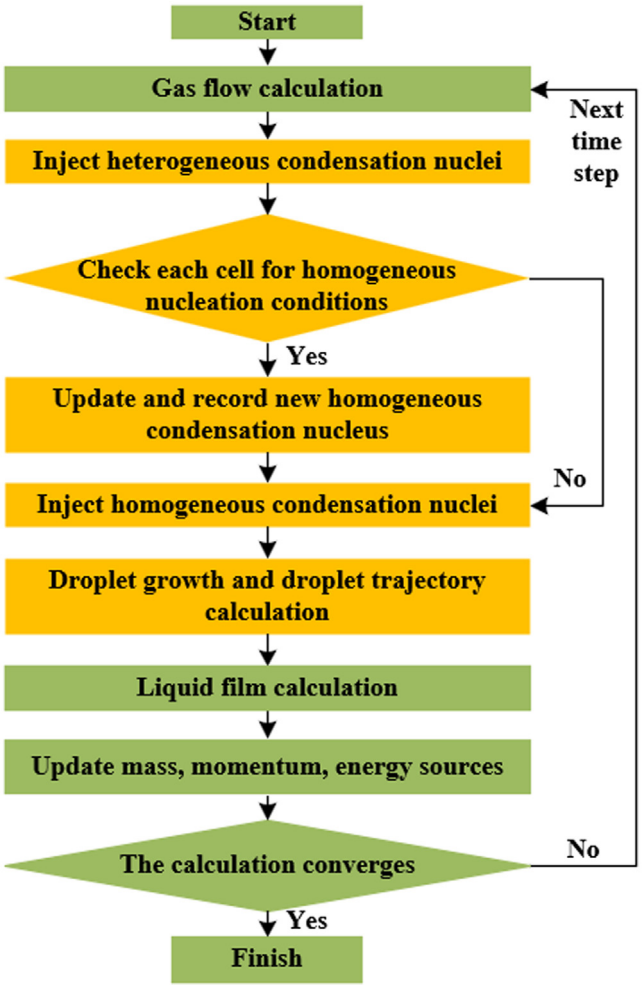

Fig. 3. Solution strategy of the modified Euler-Lagrange-Euler model.

where C is the mass coefficient, and the wave frequency (ω) is defined by

$$\omega = 0.384\sqrt{\frac{\rho_g}{\rho_f}}\frac{\rho_g\vec{v}_g^3}{\sigma} \tag{29}$$

2.4. Solution strategy

Calculations were performed using the commercial software ANSYS Fluent. The main difficulty in solving the proposed mathematical model is that the discrete phase model integrated in the software does not support real-time updateable injection of homogeneous droplets at the nucleation site, and there is no accurate heat and mass transfer model. That is, relying on ANSYS Fluent alone cannot simulate the homogeneous droplets of the Euler-Lagrange-Euler method, and even cannot accurately simulate the growth and evaporation of heterogeneous droplets, let alone interaction of homogeneous and heterogeneous droplet. User-defined functions are therefore introduced, which include the exchange of heat and mass source terms between gas, droplet, and liquid films, droplet nucleation and growth models, and recording and updating of homogeneous and heterogeneous condensation nuclei information.

Fig. 3 is the solution strategy of the proposed modified Euler-Lagrange-Euler model, the overall domain calculation is promoted through the alternate calculation of gas, droplet, and liquid film

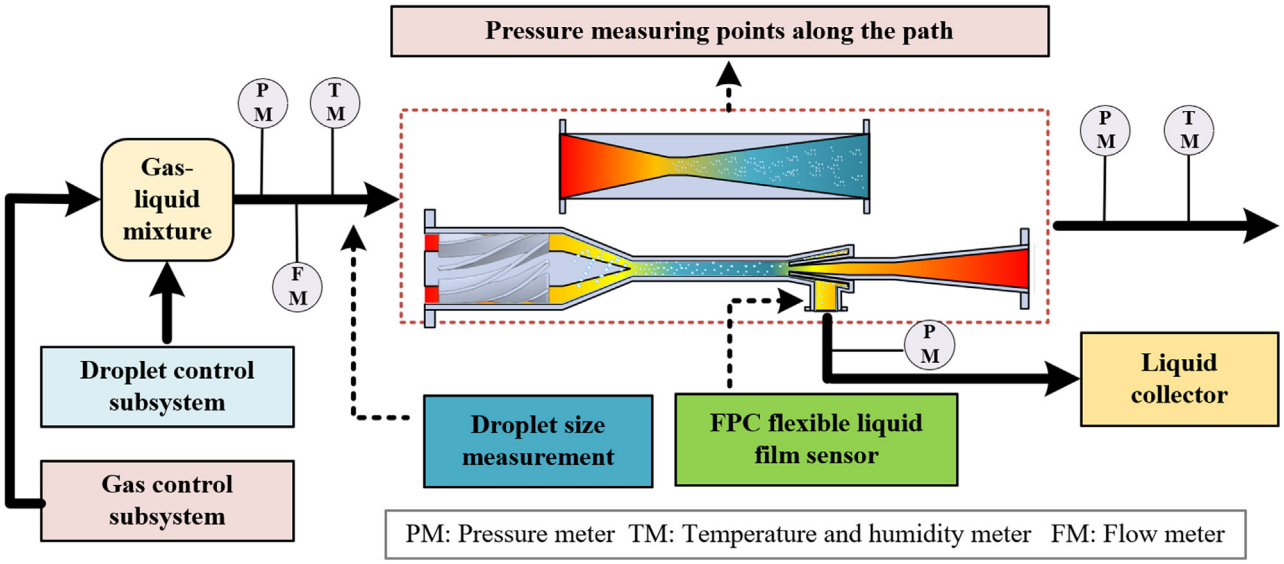

Fig. 4. Platform for supersonic nozzle and supersonic separator experiments.

until the calculation converges. The gas core calculation will provide the source term information for the liquid film, and then the liquid film calculation will provide the source term information for the gas core flow. Specifically, for discrete droplet calculations, information about heterogeneous and homogeneous condensation nuclei are recorded in external files, and droplet nuclei can be injected into the flow field at each time step by calling the file. Heterogeneous condensation nuclei have fixed information, while homogeneous condensation nuclei are continuously updated at each time step by judging whether each computing cell satisfies the homogeneous nucleation condition that the vapor supersaturation $S_s > 1$. Also, the initial file of the homogeneous condensation nuclei is empty. Homogeneous condensation nuclei begin to be generated and recorded after a period of time-step iteration, and the mass of them are determined by Eq. (14). The RSM turbulence model is adopted for its high accuracy in swirling flow [52]. The governing equations, turbulent kinetic energy equations, and turbulent dissipation rate equations are calculated using the second-order upwind equation. Pressure inlet and outlet are used as inlet and outlet boundary conditions. When a droplet hits the wall, it is collected by liquid film or ruptures and bounces off. When a droplet moves to the gas outlet, it is considered to escape. The mass balance accuracy of water is better than 1%, due to the phase change and mass exchange.

3. Experimental setup

First, to validate the proposed model, experiments were conducted. Fig. 4 is the established platform for the experiments. The gas with adjustable pressure, temperature, and humidity can be generated by the gas control subsystem, and the heterogeneous droplets with controllable particle size and concentration can be generated by the droplet control subsystem. Then the droplets and gas are mixed, the mixture flows into the supersonic nozzle or the supersonic separator and the experiment starts. Gas, droplet, and liquid film measurement sensors are distributed throughout the pipeline. All measurement results will be displayed in real-time on the host computer shown in Fig. 6 (d). The supersonic separator and supersonic nozzle used in the experiment are shown in Fig. 7 (a) and 7 (b).

The composition of the gas control subsystem is shown in Fig. 5. The gas is pressurized by air compressors, and the pressurized gas passes through oil and water eliminators in turn to remove impurities. The purified air passes through two gas storage tanks in turn for gas storage. The inlet pressure of the supersonic separator is controlled by adjusting the manual control value with a given control amount. After the gas is filtered, it enters the temperature and humidity adjustment process. The gas temperature can be controlled online by the given control amount of the gas heater with a temperature control range of 0-100°C. The gas humidity can be controlled by the water pressure automatic controller. Micro-mist droplets atomized by a high-pressure micro-mist nozzle are added to the evaporation tank. The micro-mist droplets will evaporate quickly after entering the evaporation tank, thereby adjusting the humidity of the airflow, and the humidity adjustment range is 0-100 %.

The diameter and mass flow rate of the heterogeneous droplets are controlled by the droplet control subsystem. The schematic and physical diagram of the subsystem are shown in Fig. 6 (a) and 6 (b). A filter between the water storage tank and the metering pump is to ensure the water purity. The discharge volume of the metering pump is controlled by adjusting the frequency converter. The ripple damper can effectively weaken the pipeline pressure pulsation and keep the pipeline pressure pulsation within ±5 %. The pressurized water is supplied to the micro-mist nozzle shown in Fig. 5 to adjust the gas humidity, and the micro-mist nozzle shown in Fig. 6 (a) to adjust the droplet content.

The gas parameters are measured by pressure gauges, temperature hygrometers, and vortex flowmeters. The size and concentration of the inlet heterogeneous droplets are measured by the extinction method [53] shown in Fig. 6 (c). The basic principle is that when a monochromatic light passes through a medium containing uniform suspended droplets, the outgoing light intensity will be attenuated due to the absorption and scattering of the incident light by the suspended droplets. There is a relationship between this light attenuation and size and concentration of the droplet. The film thickness at the liquid outlet is measured by a liquid film sensor based on the flexible printed circuit (FPC) [54] shown in Fig. 7 (c). Its basic structure consists of a pair of transceiver electrodes. When the surface of the electrode pair is covered with a certain thickness of the conductive liquid, and a certain potential difference is applied to stimulate, a weak current will be generated between the electrode pair, and the magnitude of the current is related to the thick-

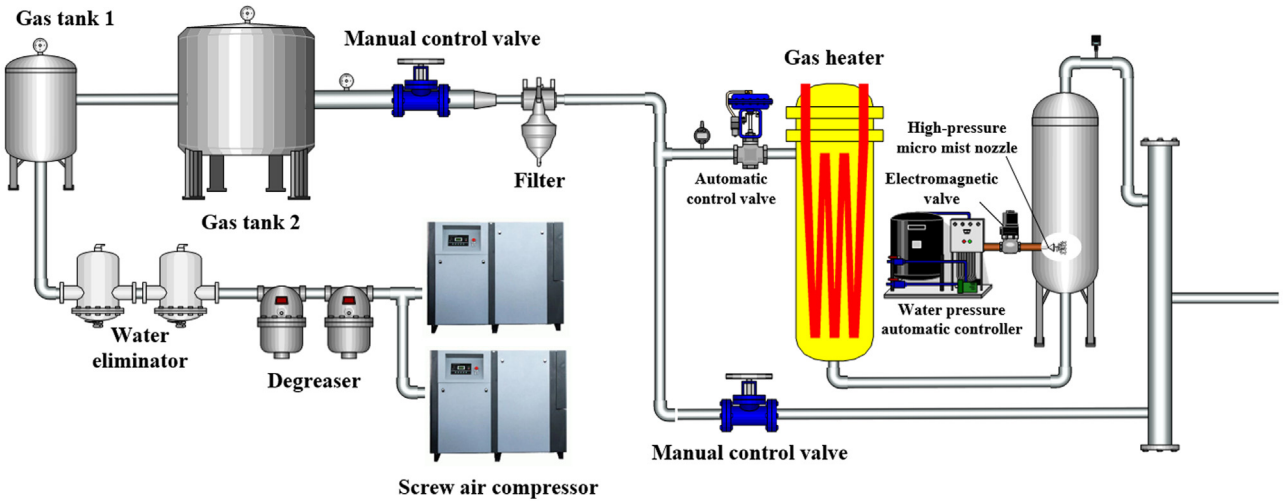

Fig. 5. Schematic of the gas control subsystem.

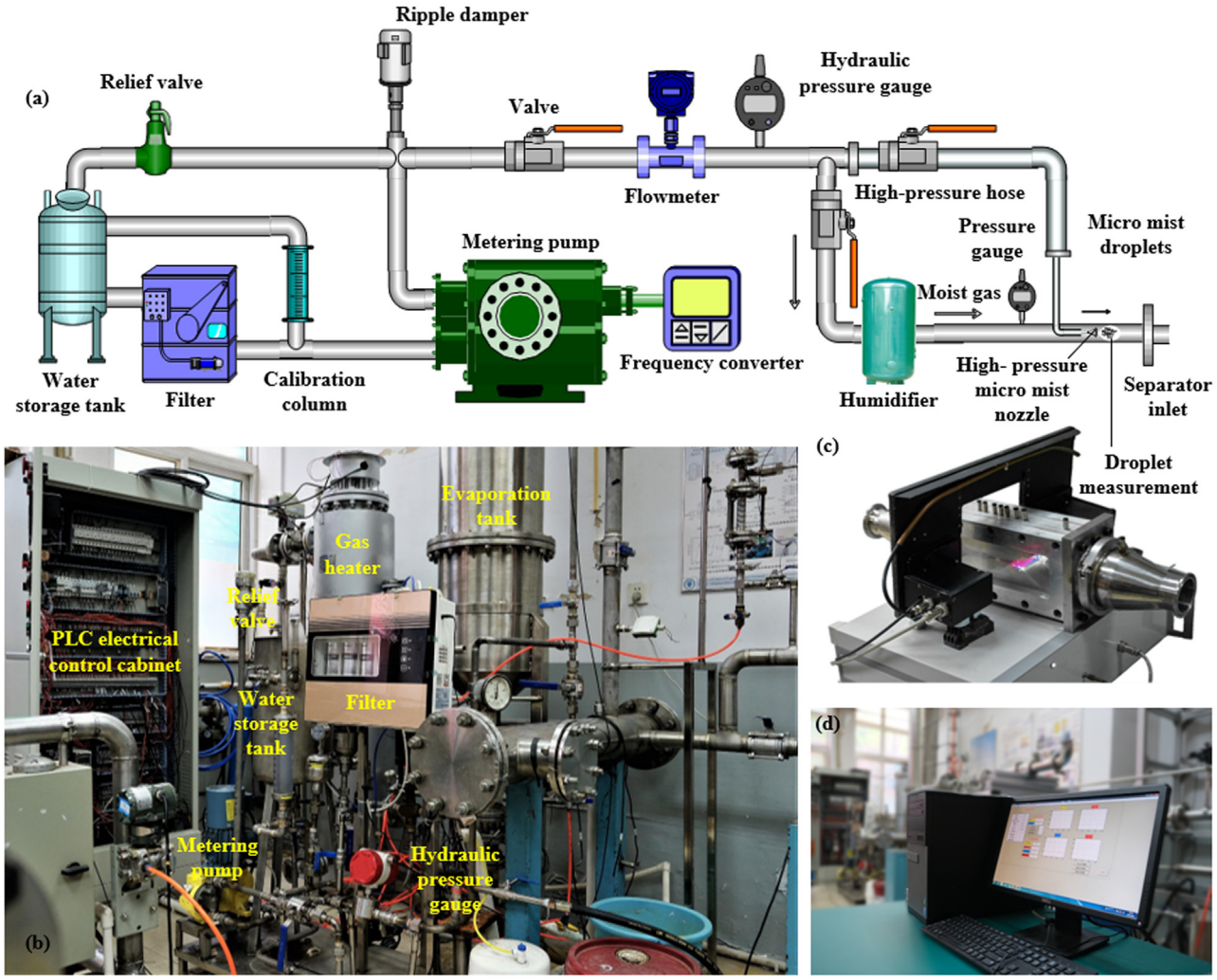

Fig. 6. Schematic and physical diagram of the heterogeneous droplet control subsystem.

ness of the conductive liquid. On this basis, supersonic nozzle experiments and supersonic separator experiments were carried out, and the experimental conditions are shown in Tables 1 and 2, where inlet pressure p_{in} and temperature T_{in} both refer to stagnation parameters. The static pressure at the outlet is a constant of 100 kPa.

4. Model validation

4.1. Validation of supersonic condensation flow

Validation of the proposed model for supersonic condensation flow was carried out. As shown in Fig. 8 (a), the total length of the

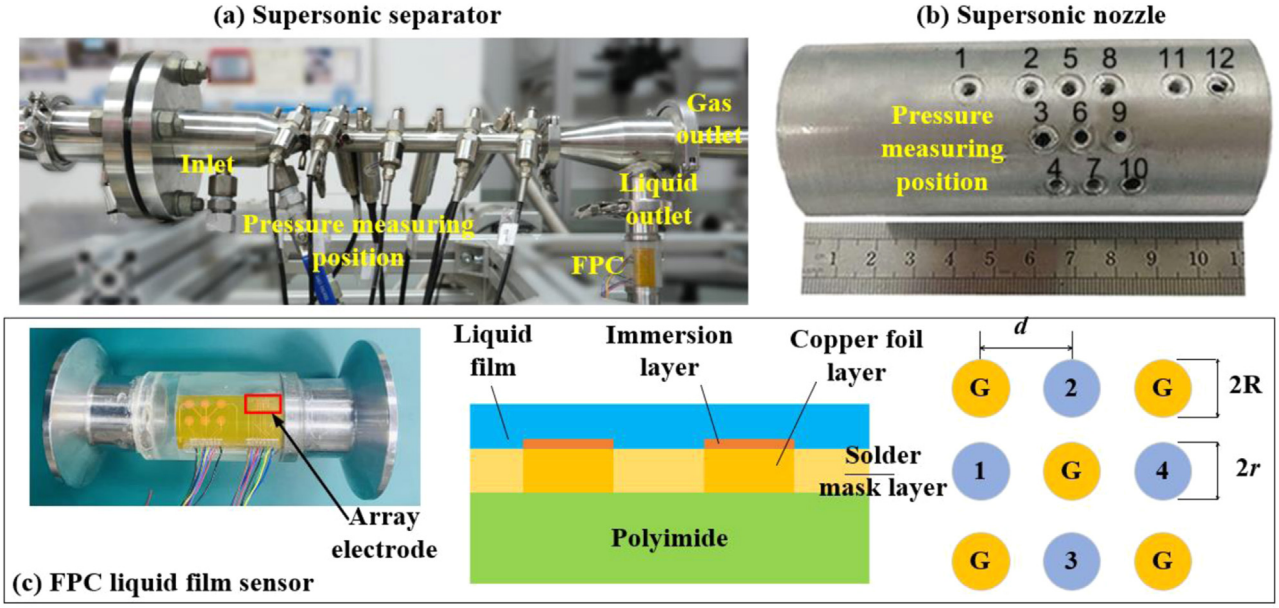

Fig. 7. The physical diagram of (a) supersonic separator and (b) the supersonic nozzle and (c) the principle of the FPC liquid film measurement method.

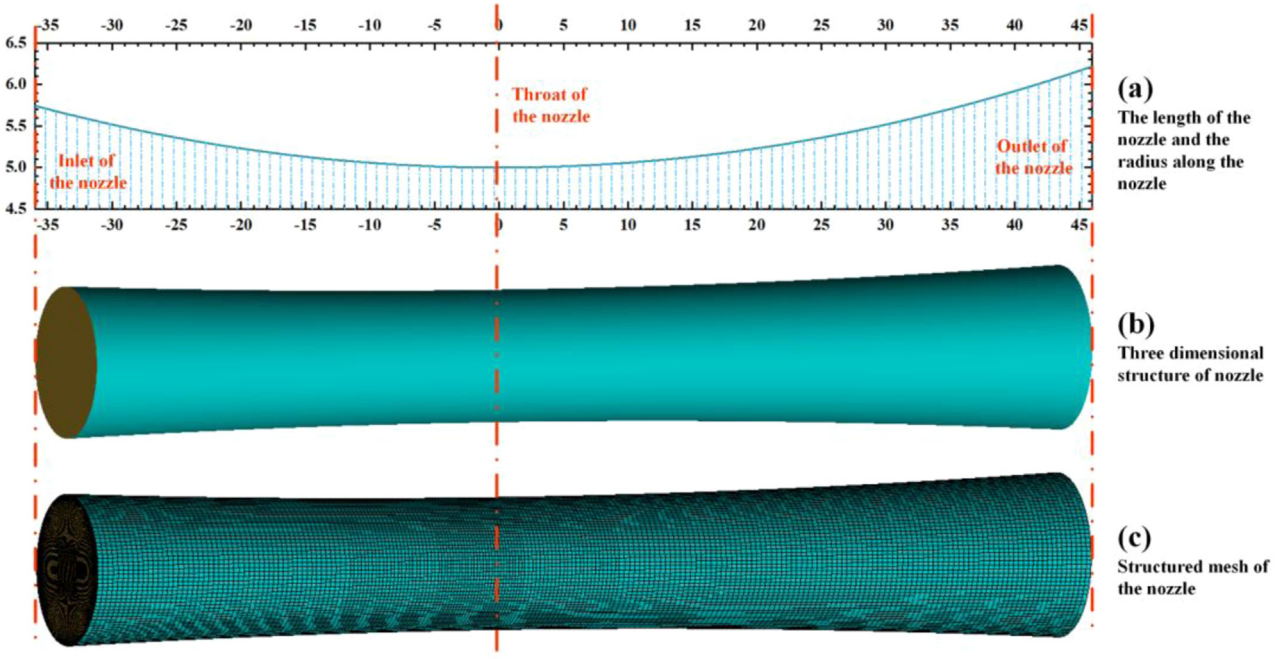

Fig. 8. Size, structure, and mesh of the supersonic nozzle.

Table 1
Conditions for supersonic nozzle experiments.

Case	p_{in} (kPa)	p_{out} (kPa)	T_{in} (K)	RH_{in} (%)
a	300	100	303	80
b	500	100	303	80
c	300	100	323	80
d	300	100	323	54
e	300	100	323	90

Table 2
Conditions for supersonic separator experiments.

Case	p_{in} (kPa)	p_{out} (kPa)	T_{in} (K)	T_{out} (K)	RH_{in} (%)	$d_{p,\,in}$ (μm)	$q_{p,\,in}$ (kg/s)
1	300	100	300	300	100	2.2	0.0001
2	300	100	300	300	100	2.2	0.0010
3	300	100	300	300	100	2.2	0.0020

used supersonic nozzle is 80 mm, and the diameters of the inlet, throat, and outlet are 11.49 mm, 10 mm, and 12.43 mm, respectively. Fig. 8 (b) and 8 (c) are the three-dimensional structure and hexahedral mesh of the supersonic nozzle. The mesh in the wall region and the throat region is refined. In the case of supersonic nozzles, accurate prediction of condensation shocks is a measure of mesh quality. In order to guarantee the accuracy of the mesh, a verification test is first performed. The Grid Convergence Index (*GCI*) is an estimate of the mesh refinement error derived based on the generalized E_R extrapolation theory [55]. To obtain the best

Table 3
The specific test results of Grid Convergence Index.

			Grid a-b 1-fine 2-medium		**Grid b-c** 2-medium 3-coarse	
	F_s	p	$\varepsilon_{1,2}$ (%)	$GCI_{1,2}$ (%)	$\varepsilon_{2,3}$ (%)	$GCI_{2,3}$ (%)
Position	3	3	0.13%	1.11%	0.75%	5.59%

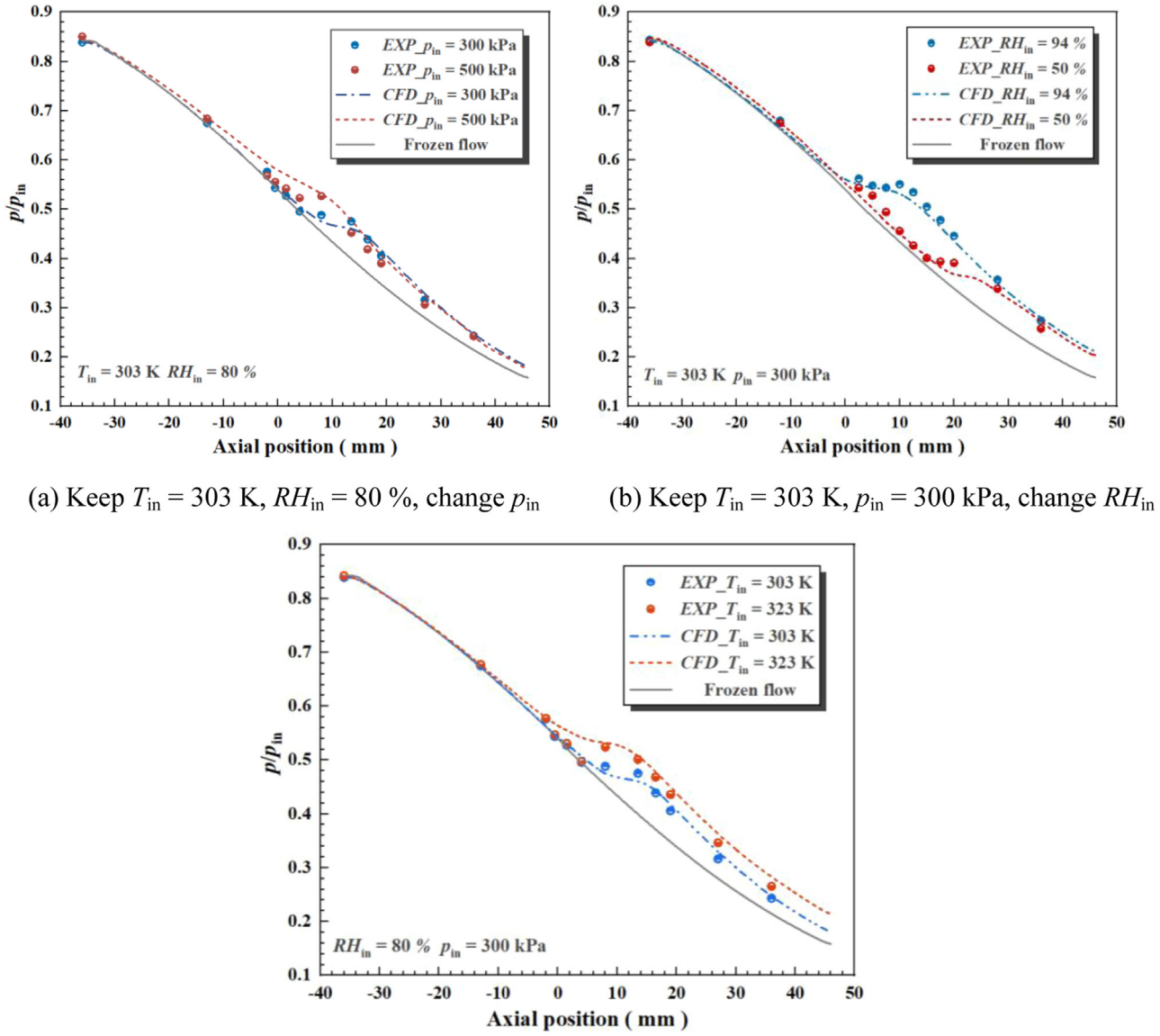

(a) Keep T_{in} = 303 K, RH_{in} = 80 %, change p_{in} (b) Keep T_{in} = 303 K, p_{in} = 300 kPa, change RH_{in}

(c) Keep RH_{in} = 80 %, p_{in} = 300 kPa, change T_{in}

Fig. 9. Experimental and simulation results of axial pressure distribution (a) Keep T_{in} = 303 K, RH_{in} = 80 %, change p_{in} (b) Keep T_{in} = 303 K, p_{in} = 300 kPa, change RH_{in} (c) Keep RH_{in} = 80 %, p_{in} = 300 kPa, change T_{in}.

computational mesh, we utilize *GCI* to calculate and analyze three sets of meshes: a: fine (1.65 million quad cells), b: medium (1.22 million quad cells), c: coarse (0.87 million quad cells). The calculation formula of *GCI* is as follows:

$$GCI = \frac{F_s|\varepsilon|}{\gamma^p - 1} \times 100\% \tag{30}$$

where F_s is the safety factor with an empirical parameter value of 3, ε is the relative error between the two grids, γ is the refinement factor ratio, and superscript p is the order of algorithm accuracy.

Taking the shock wave position as the parameter, the specific test results of *GCI* are shown in Table 3. It can be seen that the *GCI* values of Grid a-b are small and qualified, so a medium mesh (1.22 million cells) is selected, which saves the calculation cost and improves the calculation speed. It can be seen from Fig. 9 that the pressure ratio curves of the five sets of results correspond well, showing that when other conditions are constant, the increase of p_{in}, RH_{in}, or T_{in} will lead to the advance of the homogeneous condensation onset position. The proposed model can well predict the homogeneous nucleation and growth process in supersonic condensation flow.

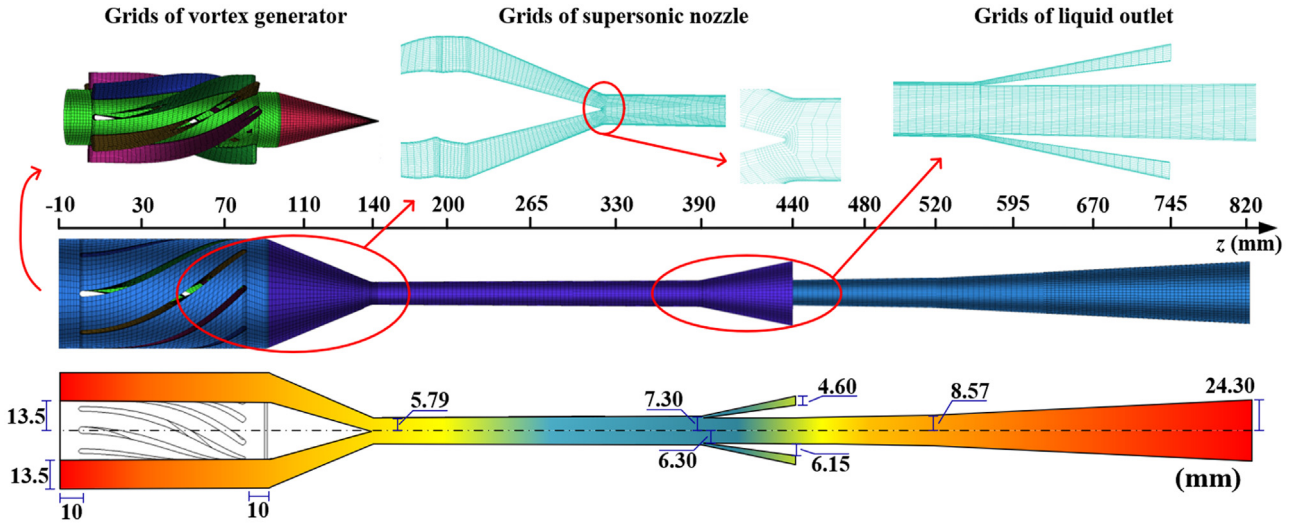

Fig. 10. Size and mesh of the supersonic separator.

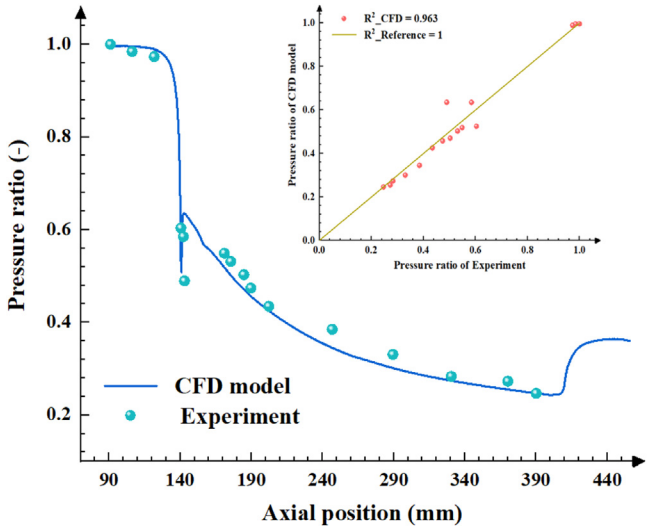

Fig. 11. Gas pressure distribution along the wall surface of the supersonic nozzle obtained by experiment and CFD model for case 1.

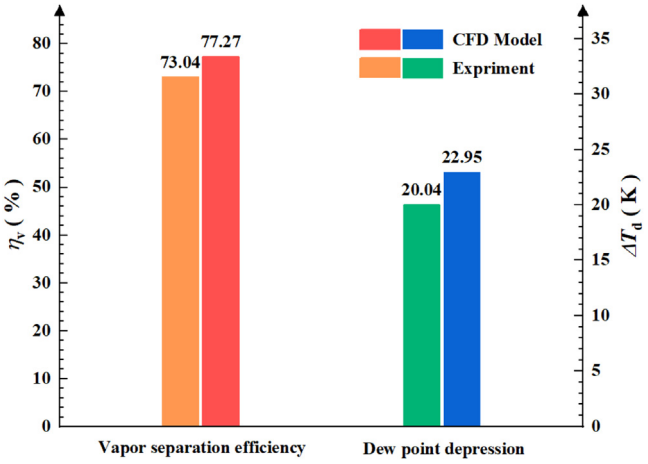

Fig. 12. Vapor separation efficiency and dew point depression obtained by experiment and CFD model for case 1.

4.2. Validation of supersonic swirling condensation annular flow

Validation of the proposed model for supersonic swirling condensation annular flow was carried out. The size and mesh of the hired supersonic separator are shown in Fig. 10. The mesh is of the structured hexahedral type, with mesh refinement near the walls and throat. By conducting GCI tests, the number of grid cells was determined to be 557560. The axial direction is defined as the z-axis direction. Fig. 11 is the gas pressure distribution obtained by the experiment and CFD model for case 1. The experimental data in the figure correspond well to the CFD data. R Square (R^2) is used to evaluate the consistency:

$$R^2 = 1 - \frac{\sum_{i=1}^{num} (a_i - b_i)^2}{\sum_{i=1}^{num} (a_i - \bar{a})^2} \tag{31}$$

where *num*, a_i, b_i, and $\bar{a}$ are the number of experimental points, experimental values, CFD model values, and experimental sample mean value, respectively. R^2 of the pressure ratio is 0.963, proving that the established CFD model has advantages in modeling the gas behavior and the gas-droplet phase change of the supersonic separator.

Fig. 12 shows the calculation results of the vapor separation efficiency η_v and dew point depression ΔT_d. η_v evaluates the change of water vapor mole fraction in the gas phase. Large η_v means good separation performance. η_v could be written as

$$\eta_v = \frac{x_{v,in} - x_{v,out}}{x_{v,in}} \times 100\% \tag{32}$$

where $x_{v,\,in}$ is the inlet vapor mole fraction, and $x_{v,\,out}$ is the vapor mole fraction at the gas outlet. ΔT_d is calculated as the difference between the inlet and the gas outlet dew point, which is expressed as

$$\Delta T_d = T_{d,in} - T_{d,out} \tag{33}$$

For case 1, the η_v and ΔT_d obtained by the CFD model are 73.07 % and 20.04 K, while the experimental values are 77.27% and 22.95 K, and the prediction errors of the two are in a reasonable range. The prediction results of the CFD model for the behavior of the liquid film can be obtained from Fig. 13. Fig. 13 (a) shows the change of film thickness at the liquid outlet of case1-3 within 120 s during the experiment. Fig. 13 (b) shows the shooting results of high-speed photography at the liquid outlet. The reason for the large fluctuations in the data is that on a long time scale, large droplets will randomly adhere to the surface of the liquid film, so filtering is required to eliminate the influence of large droplets.

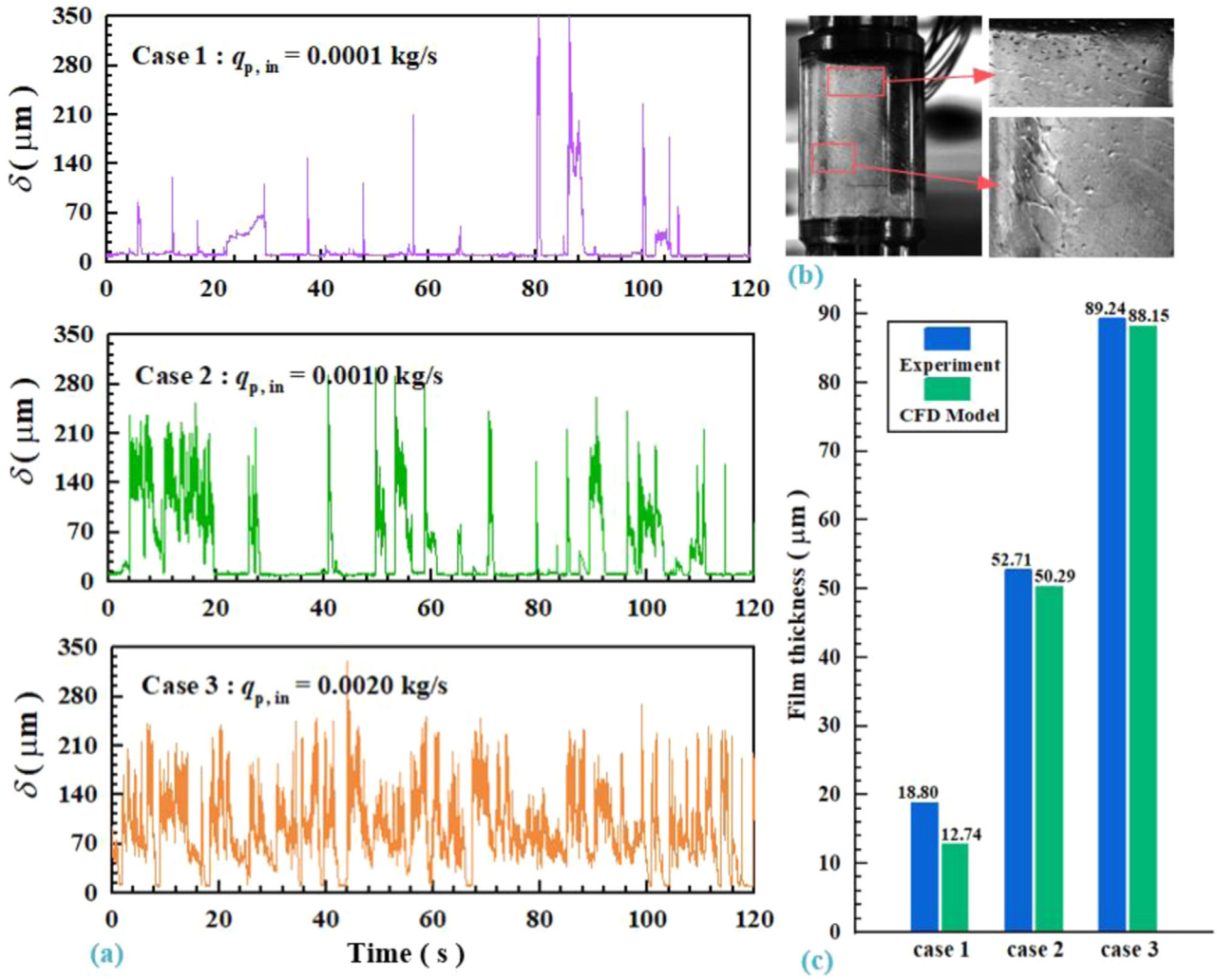

Fig. 13. Film thickness of liquid outlet obtained by experiment and CFD model.

The experimental results after a series of treatments are compared with the simulation data, and the comparison results are plotted in Fig. 13 (c). For case 1-3, the experimental film thicknesses are 18.80 μm, 52.71 μm, and 89.24 μm, respectively, while the simulated film thicknesses are 12.74 μm, 50.29 μm, and 88.15 μm, respectively. The two are in good agreement, indicating that the CFD model can also accurately predict the liquid film.

5. Results and discussion

Model validation results show that reasonable data can be obtained through the established modified Euler-Lagrange-Euler model. In this chapter, the modified Euler-Lagrange-Euler model was employed to simulate and analyze the flow feature of supersonic condensation flow and supersonic swirling condensation annular flow. Homogeneous and heterogeneous condensation flows were of particular interest. Subsequently, the research in this paper settled on a comprehensive evaluation of the separation capability of supersonic separator.

5.1. Simulation of supersonic condensation flow

5.1.1. Effect of heterogeneous droplet diameter on condensation

Fig. 14 compares the effect of the absence or presence of foreign droplets on homogeneous condensation in the flow field. It can be seen that the presence of heterogeneous growth causes the homogeneous condensation onset position to move backward. The effect of heterogeneous droplet diameter $d_{p,in}$ on condensation flow is then explored. Fig. 15 reveals the effect of changing $d_{p,in}$ on gas-phase parameters in supersonic flow. It is found that a decrease in heterogeneous droplet diameter corresponds to an increase in the pressure ratio, and also an increase in the reduced rate of y_v of the nozzle convergent section. The existence of heterogeneous droplets allows the vapor molecules to condense on the surface of the heterogeneous condensation cores immediately after the vapor state deviates from the saturation line. Therefore, when heterogeneous condensation exists, the sudden rise of the pressure is gentler than the condensation shock of only homogeneous condensation.

Fig. 16 is the distribution of axial supercooling ΔT and Sauter diameter d_{32} for different heterogeneous droplet diameters. ΔT is calculated by $\Delta T = T_{sat} - T_g$, where T_{sat} is the saturation temperature of water vapor. d_{32} is calculated as follows [56]:

$$d_{32} = \frac{\sum n_i d_p^3}{\sum n_i d_p^2} \tag{34}$$

The normalized $d_{32,het}$ in Fig. 16 is calculated as the current $d_{32,het}$ minus $d_{p,in}$. With the decrease of $d_{p,in}$, the homogeneous condensation flow weakens, and the heterogeneous condensation flow gradually becomes prominent. When $d_{p,in}$ = 1.0 μm, the vapor molecules condense directly on the condensation core pro-

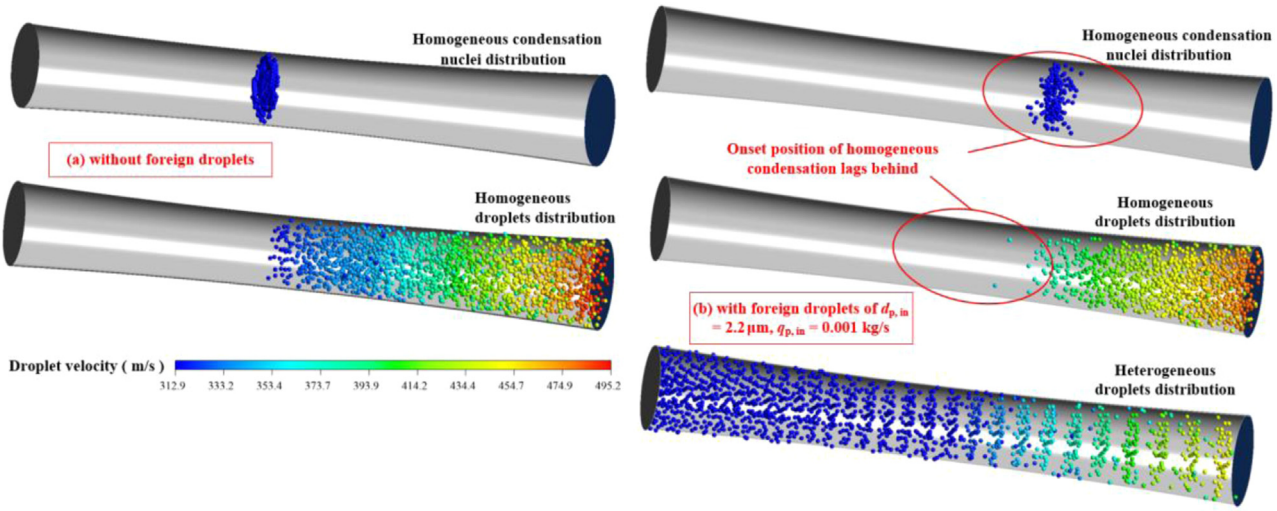

Fig. 14. Distributions of homogeneous cores, homogeneous droplets and heterogeneous droplets.

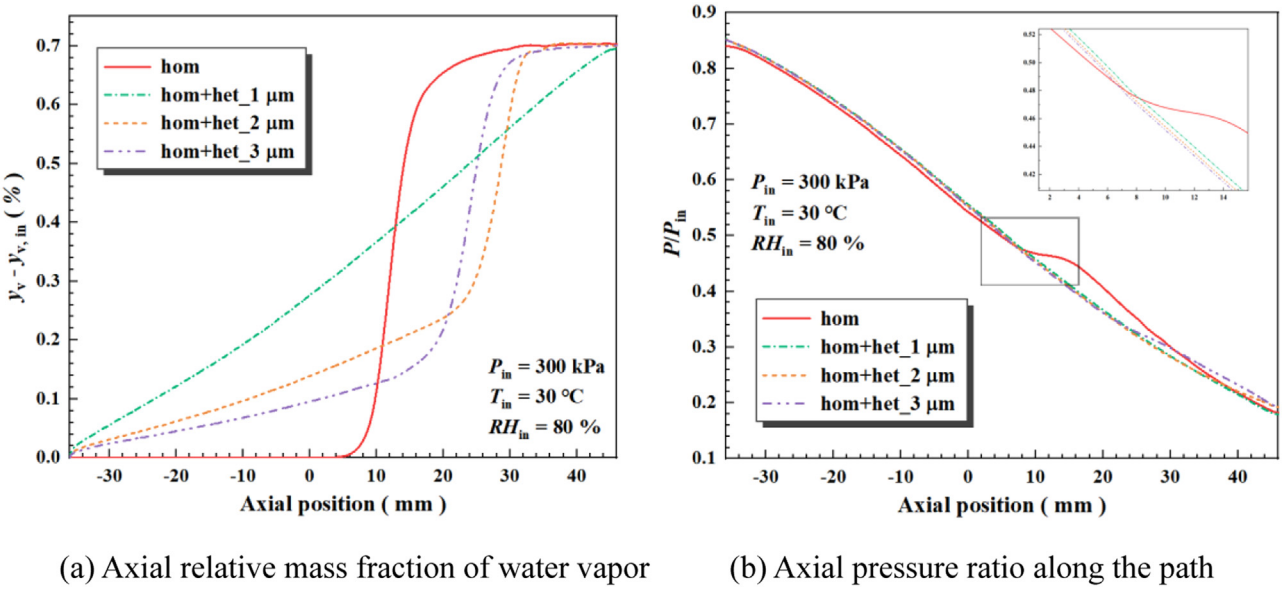

(a) Axial relative mass fraction of water vapor (b) Axial pressure ratio along the path

Fig. 15. Influence of heterogeneous droplet diameter on vapor mass fraction and pressure ratio (a) Axial relative mass fraction of water vapor (b) Axial pressure ratio along the path.

vided by the outside to achieve thermodynamic equilibrium, so the homogeneous condensation is completely suppressed, and the location of maximum supercooling is close to the nozzle outlet. When $d_{p,\,in}$ = 2 μm, the heterogeneous droplets will no longer have the ability to act as condensation cores when they grow large enough. The flow has not yet achieved thermodynamic equilibrium, so the homogeneous and heterogeneous condensation work together in the flow field, and the maximum supercooling position lies between the maximum subcooling positions for the homogeneous and $d_{p,\,in}$ = 1 μm cases.

5.1.2. Effect of heterogeneous droplet mass flow rate on condensation

The inlet heterogeneous droplet concentration also affects the supersonic condensation flow. The distribution of y_v - $y_{v,in}$ and p/p_{in} of the supersonic nozzle is shown in Fig. 17. It can be seen that an increase in $q_{p,\,in}$ corresponds to an increase in p/p_{in} and an increase in the reduced rate of y_v. Fig. 18 is the distribution of ΔT and d_{32} for different heterogeneous droplet mass flow rates. The increase of $q_{p,\,in}$ means that the vapor molecules can condensate and grow on more condensation cores, so the inhibitory effect on homogeneous condensation will be stronger. Therefore, as $q_{p,\,in}$ increases, the maximum supercooling position and homogeneous condensation onset position will be closer to the outlet. For $q_{p,\,in}$ = 0.001 kg/s, 0.0015 kg/s, and 0.002 kg/s, the homogeneous condensation onset positions are 2.5mm, 12.5mm, and 20.1mm, respectively.

5.2. Simulation of supersonic swirling condensation annular flow

5.2.1. Gas behavior in supersonic swirling flow

The generation of a high-speed swirl field is an important part to realize gas-liquid separation [57]. The pressure and Mach number distributions for the section y = 0 mm of the supersonic separator are plotted in Fig. 19 (a). When the gas flows in the convergent section of the supersonic nozzle, the temperature and pressure of the fluid will decrease as the nozzle's cross-sectional area decreases. The fluid expands so the fluid velocity increases. When the fluid flows to the nozzle throat, supersonic gas is generated with Ma = 1. Subsequently, in the divergent section of the supersonic nozzle, the gas continues to expand and the gas veloc-

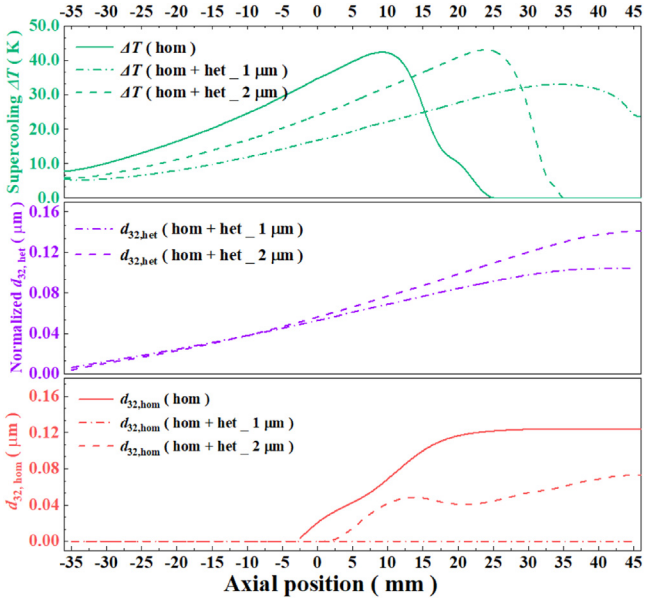

Fig. 16. Influence of heterogeneous droplet diameter on supercooling and droplet Sauter diameter.

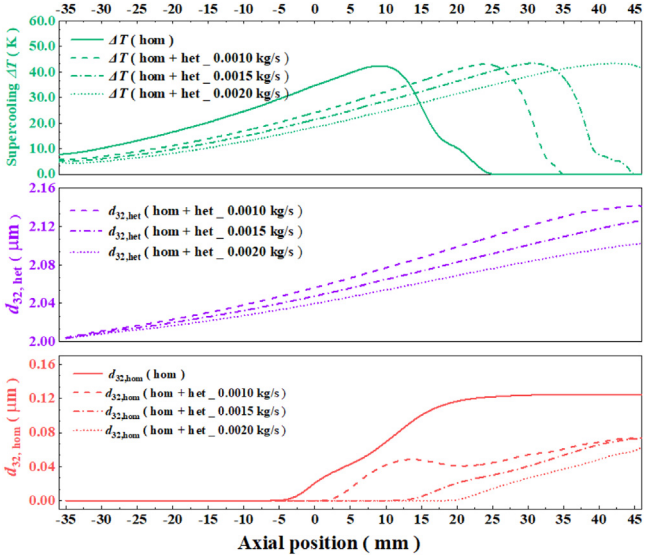

Fig. 18. Influence of heterogeneous droplet mass flow rate on supercooling and droplet Sauter diameter.

ity further increases. Before the gas pressure rises in the diffuser, the minimum pressure can reach 20 kPa, and the maximum Mach number reaches 2.3.

The dramatic reduction in pressure also creates a low-temperature environment downstream of the nozzle throat. As shown in Fig. 19 (b), a temperature drop of about 60 K facilitates the condensation of water vapor. The mass fraction of water vapor then decreases, and the lost mass is added to the condensed droplets, which makes it possible to purify the gas. In addition, the increase in the vapor mass fraction in the diffuser is because as the temperature and pressure rise, an evaporative environment is created. But overall, under the condition of case 1, the vapor mass fraction of the outlet is smaller than that of the inlet, which proves that this is an effective separation.

A strong swirl strength will reduce the Mach number and increases the static temperature inside the nozzle, thereby disrupting the expansion characteristics of the supersonic nozzle [58]. Fig. 20 is the schematic diagram of swirling gas flow in a supersonic separator. Here, a dimensionless parameter S is employed to characterize the swirl strength. S is calculated as the ratio of the tangential velocity to the axial velocity at a point. In this way, the supersonic separator used in this paper has a maximum swirl strength S = 20.6 % for case 1, with a maximum tangential velocity of 70 m/s.

5.2.2. Dynamic evolution of homogeneous and heterogeneous condensing droplets

Fig. 21 reveals the trajectories of heterogeneous and homogeneous droplets in case 1. Because of the existence of swirling flow, the heterogeneous droplets have a great probability to col-

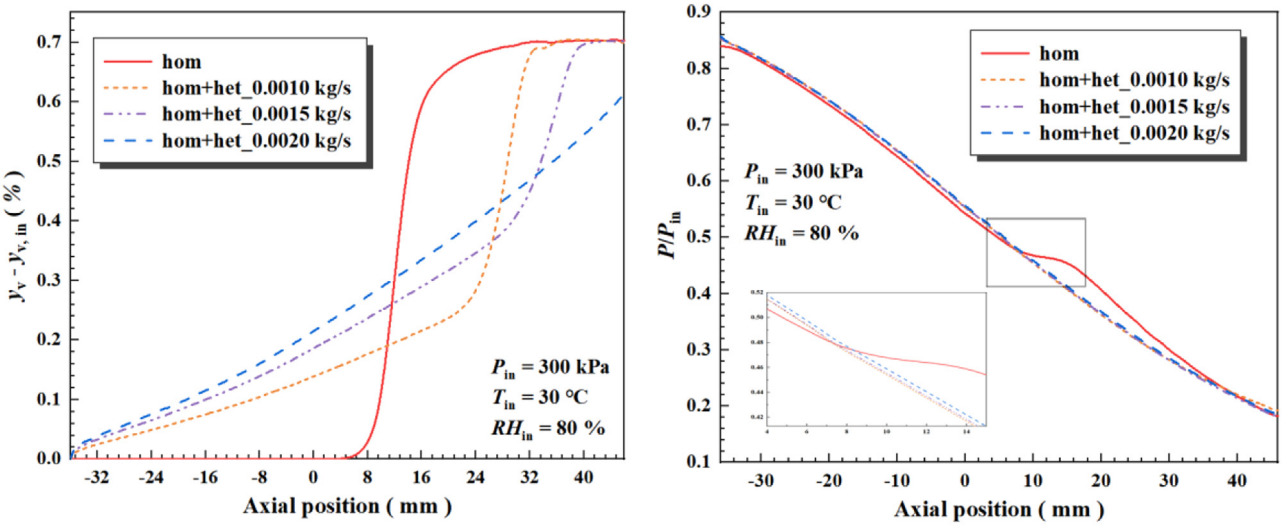

(a) Axial relative mass fraction of water vapor (b) Axial pressure ratio along the path

Fig. 17. Influence of heterogeneous droplet mass flow rate on vapor mass fraction and pressure ratio (a) Axial relative mass fraction of water vapor (b) Axial pressure ratio along the path.

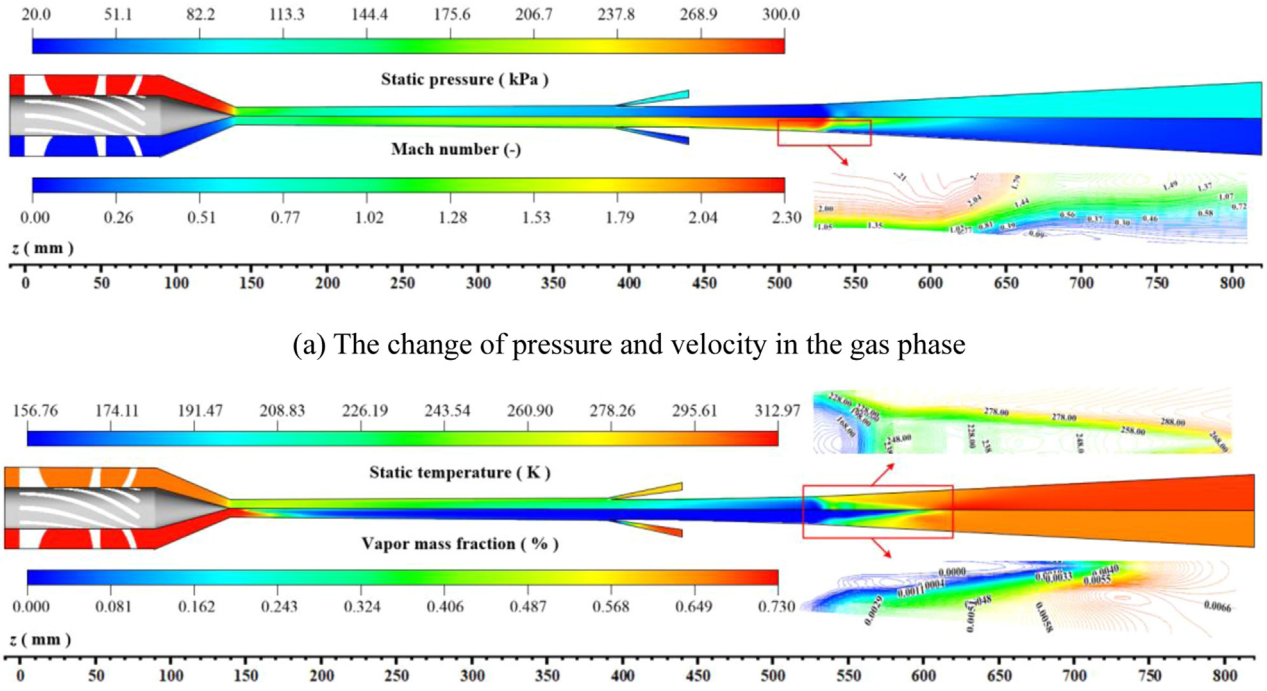

Fig. 19. Generation and evolution of supersonic gas forcase 1 (a) The change of pressure and velocity in the gas phase (b) The change of temperature and vapor mass fraction in the gas phase.

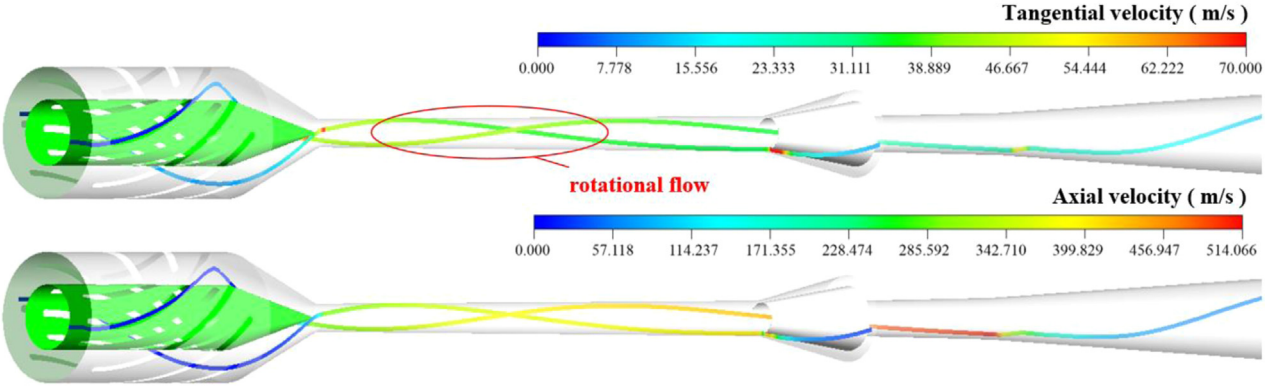

Fig. 20. Tangential and axial velocity of swirling gas for case 1.

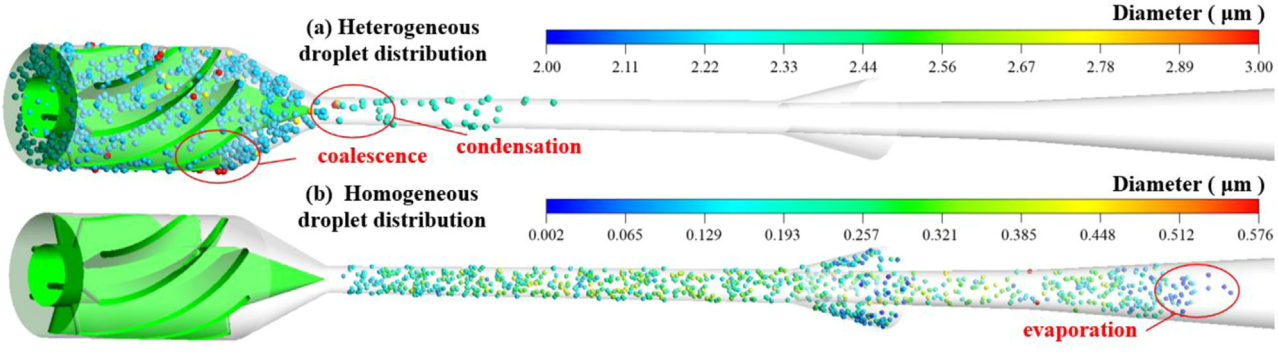

Fig. 21. Generation and evolution of droplets for case 1.

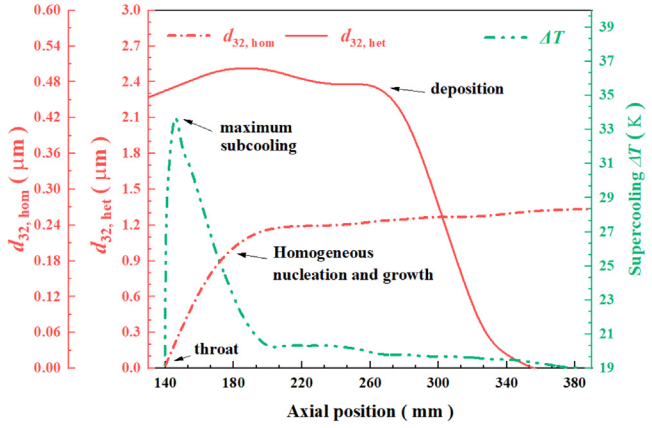

Fig. 22. Sauter diameter and supercooling distributions of the supersonic nozzle for case 1.

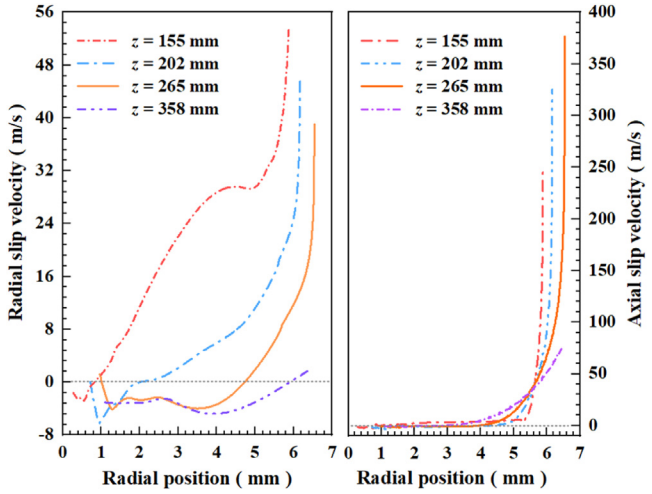

Fig. 23. Slip velocity in different axial positions for case 1.

lide and coalesce during the movement, so large droplets appear upstream of the supersonic nozzle. And under the action of the swirl strength of 20.6 %, the heterogeneous droplets have all been deposited in the middle of the divergent section of the supersonic nozzle. However, due to the limitation of the total vapor content, the homogeneous droplet diameters are generally small, the maximum is only 0.576 μm, so the swirl strength of 20.6 % cannot guarantee that all homogeneous droplets are separated. Some of the droplets escaped into the diffuser and evaporated into water vapor again during the rewarming process.

Fig. 22 shows the axial variation of the condensed droplet Sauter diameter and supercooling in the nozzle. $d_{32,\,het}$ at the nozzle throat has reached 2.33 μm, which exceeds $d_{p,\,in}$ = 2.2 μm, proving that heterogeneous condensation has occurred upstream of the throat. The occurrence of deposition is the reason for the drop in the $d_{32,\,het}$ curve. With the increase of supercooling, homogeneous droplets start to nucleate downstream of the throat. Then, the supercooling begins to decrease after reaching a peak, with the homogeneous droplets condensing and growing at a large condensation rate. At the axial position of 200 mm, this condensation rate decreases, and then $d_{32,\,hom}$ increases steadily. Further, $d_{32,\,hom}$ of 0.262 μm is occupied at the drain outlet.

The axial and radial slip velocity distribution along the radial direction of different cross-sections in case 1 is shown in Fig. 23. Overall, the axial slip velocity decreases gradually with the flow direction due to the drag force in the flow field. The radial slip velocity causes the droplet to separate from the primary gas. As the radial position increases from 0 mm to 7 mm, the radial velocity of the droplet has a process from lagging behind the radial gas velocity to surpassing the radial gas velocity, and the range of the lag will be larger when the axial position is rearward. The axial radii corresponding to the zero radial slip velocity of z = 155 mm, 202 mm, 265 mm, and 358 mm are 0.825 mm, 2.015 mm, 4.729 mm, and 5.902 mm, respectively.

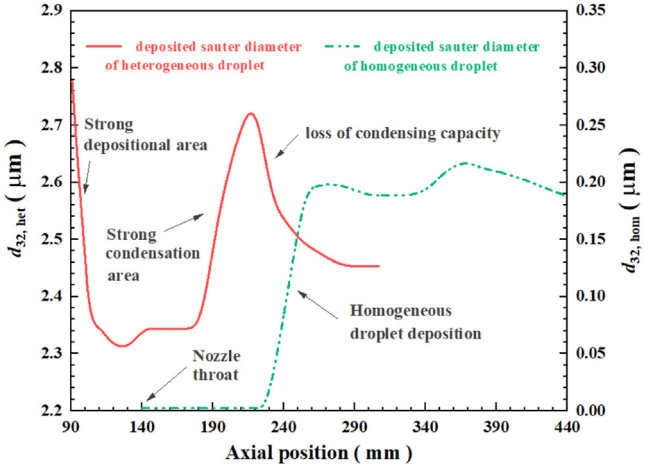

Fig. 24. Axial deposited Sauter diameter of homogeneous and heterogeneous droplets for case 1.

5.2.3. Droplet deposition and Liquid film development in annular flow

The large droplets are thrown to the wall by the swirling centrifugation and will deposit on the wall to form a thin liquid film. The deposited d_{32} along the axial path of the supersonic nozzle for case 1 is illustrated in Fig. 24. In the convergent section of the nozzle, the deposition strength caused by the swirling flow is greater than that of the condensation, so the large-diameter droplets are continuously absorbed by the liquid film, resulting in a drop of about 0.5 μm in deposited $d_{32,\,het}$. This stage corresponds to the development process of the liquid film from scratch, which can be verified in Fig. 25. At about z = 110 mm, there are fewer large-diameter droplets, so the deceleration of $d_{32,\,het}$ slows down. Further, as shown in Fig. 25, the increase of the liquid film velocity is far less than that of the gas velocity. The strong shear force between film and gas causes the mass transfer from the liquid film to the gas and droplets, resulting in a decrease in the film thickness and an increase in the entrained droplet diameter.

In the strong condensation area downstream of the throat, the water vapor is continuously converted into droplets and deposited, which is manifested as a climb of about 0.38 μm in deposited $d_{32,\,het}$. In this region, homogeneous droplet deposition also begins to appear. When the diameters of the surviving foreign core increase large enough, the heterogeneous droplets lose their ability to act as condensation cores, and their diameters will not increase, but the deposition behavior keeps going, so the deposited $d_{32,\,het}$ shows a drop of about 0.26 μm. The decreasing diameter of deposited $d_{32,\,het}$ creates an environment for homogeneous droplet deposition. The deposited $d_{32,\,hom}$ is raised to 0.2 μm, and this value is maintained until the liquid outlet.

Meanwhile, as shown in Fig. 25, during the whole process of the nozzle divergent section, the film thickness increases slowly with the flow direction under the joint work of the heat-mass transfer behaviors of deposition, entrainment, evaporation, and condensation. Then, the separation of high-speed gas greatly weakens the entrainment strength downstream of the drain outlet, so

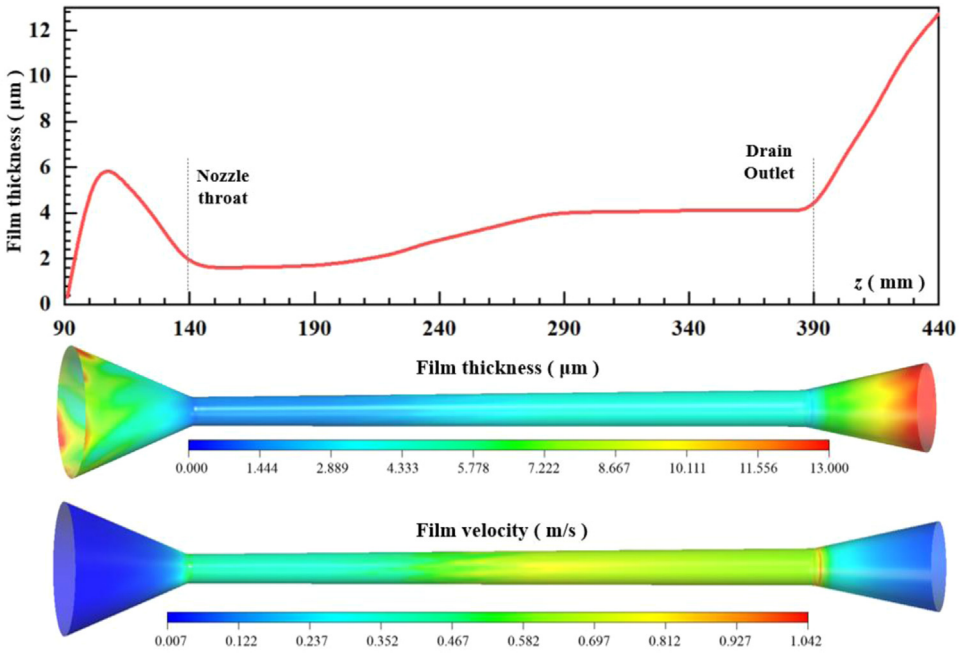

Fig. 25. Generation and evolution of liquid film for case 1.

Table 4
Effects of homogeneous condensation on separation performance of the supersonic separator.

	η_v (%)	ΔT_d (K)
Only heterogeneous condensation	86.09	29.36
Heterogeneous + homogeneous condensation	77.27	22.95

Table 5
Influence of different inlet heterogeneous droplet mass flow rate on vapor separation efficiency and dew point depression.

$q_{p,in}$ (kg/s)	η_v (%)	ΔT_d (K)
0.0001	61.39	19.03
0.0005	72.54	20.24
0.0010	77.27	22.95
0.0015	79.14	24.16
0.0020	80.34	24.99
0.0025	84.74	28.28

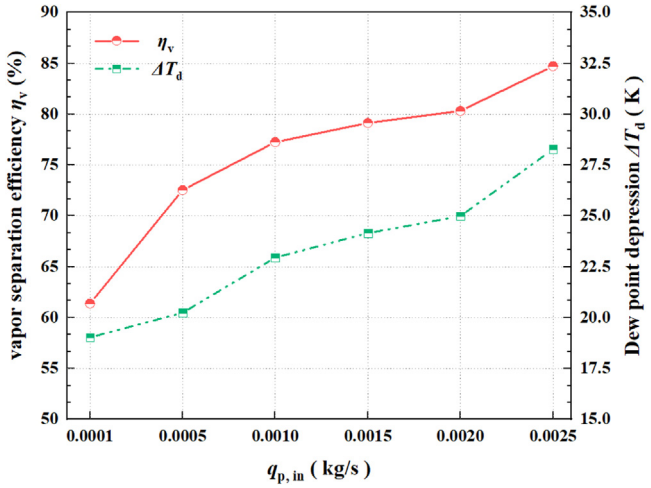

Fig. 26. Influences of different inlet heterogeneous droplet mass flow rates on vapor separation efficiency and dew point depression.

the liquid film thickness begins to increase sharply, reaching 12.74 μm at the liquid outlet.

5.2.4. Separation capacity of the supersonic separator

The effect of the combined action of homogeneous condensation and heterogeneous condensation on the separation efficiency of the supersonic separator is discussed in this section. Firstly, the effect of homogeneous condensation on the separation capacity is studied. The data in Table 4 is the difference in η_v and ΔT_d with only heterogeneous condensation and with homogeneous + heterogeneous condensation in the flow field of the supersonic separator for case 2. It can be concluded that the presence of homogeneous condensation will reduce the separation capacity of the supersonic separator due to the easy escape of small-diameter homogeneous droplets to the gas outlet. The overestimation of η_v and ΔT_d due to the presence of homogeneous condensation are 8.82 % and 6.41 K, respectively.

Table 5 and Fig. 26 are the prediction results of the separation capability of the supersonic separator using the newly established CFD model in this paper. Except for the inlet heterogeneous droplet mass flow rate, other conditions are consistent with Table 2. When $q_{p,\,in}$ increases from 0.0001 kg/s to 0.0025 kg/s, the vapor separation efficiency increases from 61.388 % to 84.737 %, and the dew point depression also increases from 19.03 K to 28.28 K. This is because the increase of $q_{p,\,in}$ means the increase of the heterogeneous condensation cores, leading to the weakening of the dominance of the homogeneous condensation, thereby improving the separation capacity of the supersonic separator.

6. Conclusion

In this paper, a modified Euler-Lagrange-Euler model considering homogeneous condensation was established to comprehensively simulate the swirling condensation annular flow in the supersonic separator. the feasibility of the CFD model was validated by the experimental comparisons. Subsequently, the CFD model was applied to the simulation of supersonic nozzle and supersonic separator, and the following conclusions were obtained:

(1) The decrease of $d_{p,\,in}$ or the increase of $q_{p,\,in}$ will increase the number of heterogeneous condensation cores, thereby inhibiting the homogeneous condensation, making the homogeneous condensation onset position and the maximum supercooling position move back, and making the condensation shock smoother.
(2) In the supersonic swirl field at the intensity of $S = 20.6$ %, the heterogeneous droplets of $d_{p,\,in} = 2.2$ μm can be completely separated by deposition, while the homogeneous droplets that have small particle sizes with a maximum of only 0.576 μm will partially escape to the diffuser, reducing the separation ability. For case 2, the loss of η_v and ΔT_d due to homogeneous condensation are 8.82 % and 6.41 K, respectively.
(3) As the radial position increases, the droplet radial velocity has a process from lagging behind the radial gas velocity to surpassing the radial gas velocity, and the range of the lag will be larger when the axial position is rearward.
(4) The heterogeneous deposited Sauter diameter has experienced a decrease of 0.5 μm, a climb of 0.38 μm, and a drop of 0.26 μm, corresponding to the strong deposition area, strong condensation area, and no heterogeneous condensation nuclei area of flow field. The third area also corresponds to the uplift of the homogeneous deposited Sauter diameter of 0.2 μm.
(5) The existence of high-speed gas and swirling droplets has a great influence on liquid film development. The gas-film high relative velocity makes the liquid film mass transfer to the gas and droplets, and the deposition of the droplets increases the mass of the liquid film.
(6) Increasing inlet droplet concentration from 0.0001 kg/s to 0.0025 kg/s can increase vapor separation efficiency and dew point depression from 61.39 % to 84.74 % and 19.03 K to 28.28 K, respectively.

In general, the established CFD model can comprehensively consider the swirling condensation annular flow in the supersonic separator and has a good predictive ability, which is expected to be applied to the optimization design of the natural gas purification process in the supersonic separator in the future.

Declaration of Competing Interest

The authors declare that they have no known competing financial interests or personal relationships that could have appeared to influence the work reported in this paper.

CRediT authorship contribution statement

Hongbing Ding: Conceptualization, Supervision, Writing – original draft, Writing – review & editing. **Yu Zhang:** Formal analysis, Investigation, Writing – review & editing. **Yan Yang:** Methodology, Investigation, Writing – review & editing. **Chuang Wen:** Supervision, Visualization, Methodology, Validation.

Data availability

No data was used for the research described in the article.

Acknowledgment

This work is supported in part by National Natural Science Foundation of China under Grant 52276159, 51876143 and 61873184.

References

[1] F. Yusuke, M. Shigeru, S. Norimasa, S. Toshiaki, Annular supersonic swirling flows with heterogeneous condensation, J. Therm. Sci. 25 (2016) 518–525.
[2] J. Tian, X. Xiao, L. Yang, C. Liu, L. Guo, Separation mechanism and dynamics characteristics of natural gas hydrate by helically coiled tube, Heat Mass Transf. 58 (2022) 1–13.
[3] M. Li, S. Fan, F. Xu, Interface coupling model of Stefan phase change during thermal dissociation of natural gas hydrate, Int. J. Heat Mass Transf. 175 (2021) 121403.
[4] I. Zavala-Guillén, J. Xamán, C. Salinas, K.A.R. Ismail, I. Hernández-Pérez, I. Hernández-López, Optical thickness effect on natural convection in a vertical channel containing a gray gas, Int. J. Heat Mass Transf. 107 (2017) 510–519.
[5] C. Wen, B. Li, H. Ding, M. Akrami, H. Zhang, Y. Yang, Thermodynamics analysis of CO2 condensation in supersonic flows for the potential of clean offshore natural gas processing, Appl. Energy 310 (2022) 118523.
[6] J. Bian, X. Cao, W. Yang, D. Guo, C. Xiang, Prediction of supersonic condensation process of methane gas considering real gas effects, Appl. Therm. Eng. 164 (2020) 114508.
[7] J. Bian, X. Cao, W. Yang, X. Song, C. Xiang, S. Gao, Condensation characteristics of natural gas in the supersonic liquefaction process, Energy 168 (2019) 99–110.
[8] C. Wen, H. Ding, Y. Yang, Optimisation study of a supersonic separator considering nonequilibrium condensation behaviour, Energy Convers. Manag. 222 (2020) 113210.
[9] A.F. Bolaños-Acosta, J.C. Restrepo, J.R. Simões-Moreira, Two semi-analytical approaches for solving condensation shocks in supersonic nozzle flows, Int. J. Heat Mass Transf. 173 (2021) 121212.
[10] C. Wen, N. Karvounis, J.H. Walther, H. Ding, Y. Yang, Non-equilibrium condensation of water vapour in supersonic flows with shock waves, Int. J. Heat Mass Transf. 149 (2020) 119109.
[11] J. Chen, W. Jiang, X. Lai, X. Cao, J. Bian, Z. Bi, Study on the influence of wall–mounted cyclone on the purification and separation performance of supersonic separator, Chem. Eng. Process. Process Intensif. 150 (2020) 107898.
[12] X. Cao, D. Guo, W. Sun, P. Zhang, G. Ding, J. Bian, Supersonic separation technology for carbon dioxide and hydrogen sulfide removal from natural gas, J. Clean. Prod. 288 (2021) 125689.
[13] Y. Wang, Analysis for spiral vortex and effect of profile of nozzle and swirler on performance of supersonic separator, Chem. Eng. Process. Process Intensif. 147 (2020) 107676.
[14] D. Majidi, F. Farhadi, Supersonic separator's dehumidification performance with specific structure: experimental and numerical investigation, Appl. Therm. Eng. 179 (2020) 115551.
[15] C. Ma, Y. Wang, Y. Yu, W. Ren, D. Hu, Structure improvements and performance study of Supersonic Separation device with reflux channel, Chem. Eng. Process. Process Intensif. 138 (2019) 73–85.
[16] H. Ding, C. Sun, C. Wen, Z. Liang, The droplets and film behaviors in supersonic separator by using three-field two-fluid model with heterogenous condensation, Int. J. Heat Mass Transf. 184 (2022) 122315.
[17] Y. Liu, H. Wang, I. Ayub, F. Yang, Z. Wu, Z. Zhang, A variable cross-section annular fins type metal hydride reactor for improving the phenomenon of inhomogeneous reaction in the thermal energy storage processes, Appl. Energy 295 (2021) 117073.
[18] Y. Deng, L. Zhang, H. Hou, B. Yu, D. Sun, Modeling and simulation of the gas-liquid separation process in an axial flow cyclone based on the Eulerian-Lagrangian approach and surface film model, Powder Technol. 353 (2019) 473–488.
[19] A.V. Murashkina, D.S. Kuliukhina, A.D. Averin, A.S. Abel, E.N. Savelyev, B.S. Orlinson, et al., A comparison of homogeneous and heterogeneous copper catalyzed arylation of amines, Mendeleev Commun. 32 (2022) 91–93.
[20] J. Han, J. Feng, T. Hou, W. Chen, X. Peng, Numerical and experimental study on gas-water separators for a PEMFC system, Int. J. Green Energy 18 (2021) 490–502.
[21] I. Pađen, Z. Petranović, W. Edelbauer, M. Vujanović, Numerical modeling of spray secondary atomization with the Euler-Eulerian multi-fluid approach, Comput. Fluids 222 (2021) 104919.
[22] S. Dykas, W. Wróblewski, Numerical modelling of steam condensing flow in low and high-pressure nozzles, Int. J. Heat Mass Transf. 55 (2012) 6191–6199.
[23] S. Dykas, W. Wróblewski, Two-fluid model for prediction of wet steam transonic flow, Int. J. Heat Mass Transf. 60 (2013) 88–94.
[24] Y. Liu, X. Cao, J. Yang, Y. Li, J. Bian, Energy separation and condensation effects in pressure energy recovery process of natural gas supersonic dehydration, Energy Convers. Manag. 245 (2021) 114557.
[25] S.H.R. Shooshtari, A. Shahsavand, Optimal operation of refrigeration oriented supersonic separators for natural gas dehydration via heterogeneous condensation, Appl. Therm. Eng. 139 (2018) 76–86.
[26] H. Ding, C. Sun, C. Wang, C. Wen, Y. Tian, Prediction of dehydration performance of supersonic separator based on a multi-fluid model with heterogeneous condensation, Appl. Therm. Eng. 171 (2020) 115074.
[27] Z. Huang, H. Yan, L. Liu, H. Gong, P. Zhou, Numerical modeling of reactive bubbly flows based on Euler-Lagrange approach, Chem. Eng. Sci. 239 (2021) 116640.
[28] C. Wen, X. Cao, Y. Yang, J. Zhang, Evaluation of natural gas dehydration in supersonic swirling separators applying the discrete particle method, Adv. Powder Technol. 23 (2012) 228–233.
[29] X. Liu, Z. Liu, Y. Li, Investigation on separation efficiency in supersonic separator with gas-droplet flow based on DPM approach, Sep. Sci. Technol. 49 (2014) 2603–2612.
[30] B. Bai, X. Li, S. Li, Computation of supersonic branching flow with aerosol particle separation, AIAA J. 54 (2016) 2069–2076.

[31] Y. Yang, C. Wen, CFD modeling of particle behavior in supersonic flows with strong swirls for gas separation, Sep. Purif. Technol. 174 (2017) 22–28.
[32] Y. Wang, Y. Yu, D. Hu, D. Xu, L. Yi, Y. Zhang, et al., Improvement of drainage structure and numerical investigation of droplets trajectories and separation efficiency for supersonic separators, Chem. Eng. Process. Process Intensif. 151 (2020) 107844.
[33] Y. Kobashi, Y. Zama, T. Kuboyama, Modeling wall film formation and vaporization of a gasoline surrogate fuel, Int. J. Heat Mass Transf. 147 (2020) 119035.
[34] Z. Liu, C. Tao, S. Yuan, W. Wang, M. Tamaddon, L. Ng, et al., Eularian wall film model for predicting dynamic cell culture process to evaluate scaffold design in a perfusion bioreactor, Med. Novel Technol. Devices 13 (2022) 100104.
[35] H. Li, H. Anglart, Prediction of dryout and post-dryout heat transfer using a two-phase CFD model, Int. J. Heat Mass Transf. 99 (2016) 839–850.
[36] W. Chen, Y. Chen, W. Zhang, S. He, B. Li, J. Jiang, Paint thickness simulation for robotic painting of curved surfaces based on Euler–Euler approach, J. Braz. Soc. Mech. Sci. 41 (2019) 1–9.
[37] T. Yue, J. Chen, J. Song, X. Chen, Y. Wang, Z. Jia, et al., Experimental and numerical study of Upper Swirling Liquid Film (USLF) among Gas-Liquid Cylindrical Cyclones (GLCC), Chem. Eng. J. 358 (2019) 806–820.
[38] Y. Liu, J. Cui, W.Z. Li, A two-phase, two-component model for vertical upward gas–liquid annular flow, Int. J. Heat Fluid Flow 32 (2011) 796–804.
[39] Y. Liu, W.Z. Li, SL. Quan, A self-standing two-fluid CFD model for vertical upward two-phase annular flow, Nucl. Eng. Des. 241 (2011) 1636–1642.
[40] D. Adechy, RI. Issa, Modelling of annular flow through pipes and T-junctions, Comput. Fluids 33 (2004) 289–313.
[41] S. Yuan, Y. Fan, B. Chen, J. Li, L. Gao, S. Zhang, Forming and stripping of the wall film and the influence on gas–liquid separation, Asia-Pac. J. Chem. Eng. 15 (2020) e2447.
[42] H. Ounis, G. Ahmadi, J.B. McLaughlin, Brownian diffusion of submicrometer particles in the viscous sublayer, J. Colloid Interface Sci. 143 (1991) 266–277.
[43] P. O'Rourke, Collective Drop Effects on Vaporizing Liquid Sprays, Princeton University, 1981.
[44] T. Frank, Parallele Algorithmen für die Numerische Simulation Dreidimensionaler, Disperser Mehrphasenströmungen und Deren Anwendung in der Verfahrenstechnick, Chemnitz, Techn. Univ., Habil-Schr. Shaker Verlag, 2002.
[45] H. Ding, Y. Zhang, C. Sun, Y. Yang, C. Wen, Numerical simulation of supersonic condensation flows using Eulerian-Lagrangian and Eulerian wall film models, Energy 258 (2022) 124833.
[46] A. Kantrowitz, Nucleation in very rapid vapor expansions, J. Chem. Phys. 19 (1951) 1097–1100.
[47] M. Marcus, R. Hunt, The flow of wet steam in a one-dimensional nozzle, Int. J. Numer. Methods Eng. 44 (1999) 1807–1821.
[48] MooreTwo-Phase Steam Flow in Turbines and Separators, Hemisphere Publishing Co., 1976.
[49] J. Reznickova, R. Petrychkovych, J. Vejrazka, K. Setnickova, P. Uchytil, Gas separation ability of the liquid bubble film, Sep. Purif. Technol. 166 (2016) 26–33.
[50] W. Xianmao, C. Huajian, C. Michael, C. Tenglong, W. Jun, Prediction of falling film evaporation on the AP1000 passive containment cooling system using ANSYS FLUENT code, Ann. Nucl. Energy 95 (2016) 168–175.
[51] P.E. Springer, T.A. Zawodzinski, S. Gottesfeld, Polymer Electrolyte Fuel Cell Model, J. Electrochem. Soc. 138 (2019) 2334.
[52] A.J. Hoekstra, J.J. Derksen, H.E.A. Van Den Akker, An experimental and numerical study of turbulent swirling flow in gas cyclones, Chem. Eng. Sci. 54 (1999) 2055–2065.
[53] M. Jiang, X. Liu, J. Han, Z. Wang, M. Xu, Influence of particle properties on measuring a low-particulate-mass concentration by light extinction method, Fuel 286 (2021) 119460.
[54] L. Zhang, X. Qu, S. Lu, X. Wang, L. Lin, Z. Zhao, et al., Temperature and strain monitor of COPV by buckypaper and MXene sensor combined flexible printed circuit, Int. J. Hydrog. Energy 47 (2022) 4211–4221.
[55] P.J. Roache, Quantification of uncertainty in computational fluid dynamics, Annu. Rev. Fluid Mech. 29 (1997) 123–160.
[56] Y. Yoo, D. Han, J. Hong, H. Sung, A large eddy simulation of the breakup and atomization of a liquid jet into a cross turbulent flow at various spray conditions, Int. J. Heat Mass Transf. 112 (2017) 97–112.
[57] J. Bian, X. Cao, L. Teng, Y. Sun, S. Gao, Effects of inlet parameters on the supersonic condensation and swirling characteristics of binary natural gas mixture, Energy 188 (2019) 116082.
[58] C. Wen, X. Cao, Y. Yang, J. Zhang, Swirling effects on the performance of supersonic separators for natural gas separation, Chem. Eng. Technol. 34 (2011) 1575–1580.